Chapter 2
Characterization Methodologies of Thermal Management Materials

Abstract The materials selection for thermal management of electronic packaging is influenced by thermal, electrical, physical and thermomechanical requirements of the device and its surrounding electrical system and by the environment to which the device will be exposed. The reliability of the finished device and electric system will depend not only on the characteristics of the individual materials but also on the interaction of package and thermal management materials at interfaces during exposure to such stresses as thermal gradients, temperature cycling, moisture, and contamination. This chapter will introduce general characterization methodologies of thermal management materials for assessing performance and reliability of electronic packaging, including thermal properties, electrical properties, thermomechanical analysis, as well as material microstructure and interface characterization, surface finish and contact interface compatibility, and reliability analysis and environmental evaluation.

Thermal Properties and Measurement Techniques

The major thermal properties involved in the characterization of the thermal management materials for electronic packaging include thermal conductivity and diffusivity, specific heat capacity, coefficient of thermal expansion (CTE), and thermal shock resistance. A variety of measurement techniques have been developed to evaluate these properties for thermal management materials, here mainly focusing on some classic testing methods.

Thermal Conductivity and Diffusivity

The accurate measurement and characterization of the thermal conductivity of bulk materials can pose many challenges. For instance, loss terms of the heat input intended to flow through the sample usually exist and can be most difficult to quantify. Many testing methods exist with an accuracy of within 5%, such as the

X.C. Tong, *Advanced Materials for Thermal Management of Electronic Packaging*, Springer Series in Advanced Microelectronics 30,
DOI 10.1007/978-1-4419-7759-5_2,

steady-state technique, the 3ω technique, and the thermal diffusivity measurement (Uher 2005). Each of these techniques has its own advantages as well as its inherent limitations, with some techniques more appropriate to specific sample geometry, such as the 3ω technique for thin films (this method will be discussed in the section "Thermal Characterization of Micro/Nanomaterials"). This section will focus on the measurement techniques that are more appropriate for bulk-like solid-state materials.

Thermal conductivity, k, is the property of a material that indicates its ability to conduct heat. It can be defined by first order Fourier–Biot equation as the quantity of heat, ΔQ, transmitted during time Δt through a thickness Δx, in a direction normal to a surface of area A, due to a temperature difference ΔT, under steady state conditions and when the heat transfer is dependent only on the temperature gradient. That is

$$k = \frac{\Delta Q}{\Delta t} \times \frac{1}{A} \times \frac{\Delta x}{\Delta T}. \tag{2.1}$$

Thermal diffusivity, α, is the rate at which a temperature disturbance on one side of the body travels to another part of the body, defined by second order Fourier–Biot equation as

$$\frac{\partial T(r,t)}{\partial t} = \alpha \nabla^2 T(r,t). \tag{2.2}$$

Thermal conductivity and thermal diffusivity are related by

$$k = \alpha \rho C_p, \tag{2.3}$$

where k is thermal conductivity in W/m K; α is thermal diffusivity in m^2/s; ρ is material density in kg/m^3; and C_p is specific heat capacity in J/kg K. At high temperatures, or when the material is available only in small sizes, α, ρ, and C_p are often measured to determine thermal conductivity k. This kind of measurement method is classified as transient method, as discussed later in this chapter.

Thermal conductivity approximately tracks electrical conductivity for metals according to the Wiedemann–Franz law, as freely moving valence electrons transfer not only electric current but also heat energy. However, the general correlation between electrical and thermal conductance does not hold for other nonmetal materials due to the increased importance of phonon carriers for heat in nonmetals. For example, highly electrically conductive silver is less thermally conductive than diamond, which is an electrical insulator. Additionally, thermal conductivity depends on many properties of a material, notably its structure and temperature.

As shown in Figure 2.1 and Table 2.1, a number of techniques have been developed to measure thermal conductivity and thermal diffusivity, each of them suitable for a limited range of materials, depending on the thermal properties and the medium temperature (Maglić et al. 1984, 1992). The exist measurement

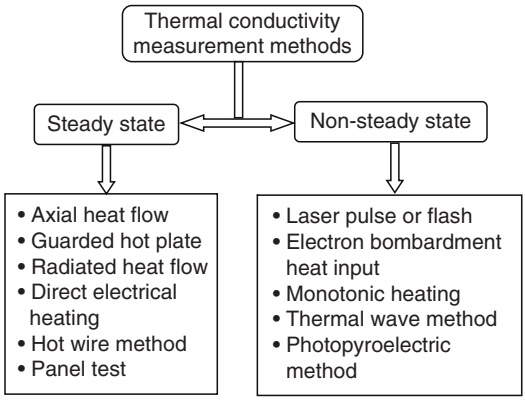

Fig. 2.1 Illustration of typical thermal conductivity measurement techniques

methods can be divided into two classes: steady-state and non-steady-state or transient methods. A distinction can be made between steady-state and transient techniques. The steady-state techniques generally perform a measurement when the temperature of the material that is measured does not change with time. This makes the signal analysis straightforward. The disadvantage is that it usually takes a well-engineered experimental setup. Comparably, the transient techniques perform a measurement during the process of heating up. The advantage is that measurements can be made relatively quickly because there is no need to wait for a steady-state situation. The disadvantage is that the mathematical analysis of the data is in general more difficult.

For conductivity measurement, steady-state methods (up to 1,200 K) and pulse methods (in particular over 1,500 K) are usually used. For instance, if the material under test is a conductor, the specimen can be self heated by passing of an electric current. Transient methods are usually preferred for diffusivity measurement. Measuring diffusivity requires an accurate recording of the time dependence of temperature following a transient or periodic temperature perturbation at a specimen boundary. As a consequence of the wide ranges of thermal property, there is no single method of measurement that can be used for measurement of either property, in particular thermal conductivity. To obtain acceptable values for the measured property, the material type and its range of property value over its operational temperature range will particularly influence the type of method used and the size and conjunction of the test specimen and apparatus.

Therefore, thermal conductivity is measured by steady-state techniques and thermal diffusivity by transient techniques. It is possible to use some of the latter in a modified way to also measure thermal conductivity, or converse the diffusivity data to the conductivity data. However, a measurement method has to be selected depending on the following criteria: (1) appropriate sample size and shape; (2) applicable temperature range, which is limited for individual techniques; (3) suitable thermal conductivity range, because low conductivity materials such as insulating materials or foams need different methods than for high conductivity materials such as metals.

Table 2.1 Thermal conductivity and diffusivity measurement methods

Measurement method	Specimen material type	Temperature range (K)	Conductivity range (W/m K)	Uncertainty (%)	Advantages	Disadvantages
Axial heat flow	Metals and metallic alloys; cylindrical shape specimen	90–1,300	10–500	0.5–2.0	High accuracy; utilize electrical resistivity for heating source	Heat losses above ~500 K
Direct electrical heating	Wires, rods, tubes of electrical conductors	400–3,000	10–200	2.0–5.0	Wide temperature coverage. Fast and use electric properties	Complex equipment
Radial heat flow	Solids and powders in cylindrical form	298–2,600	0.01–200	3.0–15	Good accuracy with wide temperature coverage	Large specimens
Guarded hot plate	Solid, opaque, insulators	80–1,500	0.0001–1.0	2.0–5.0	Apply to wide range of materials. High accuracy	Complex costly slow (3–12 h)
Hot wire method	Refractory materials	298–1,800	0.02–2	5.0–15	Small size probe; drop in specimen	Apply to low conductivity materials
Panel test	Refractory materials	600–1,600	0.05–15	15	Simplicity	High temperature gradients; slow measuring
Laser flash	Solids, liquid metals; polymers; ceramics. Disk specimen 6–16 mm in diameter	100–3,300	0.1–1,500	1.5–5	Wide temperature coverage. Simple, rapid measurement for thermal diffusivity	Not convenient for translucent materials. Complex error analysis
Thermal wave	Solids, liquid metals, gases. Specimen shape: rods, cylinders	60–1,300	0.5–500	1.0–9	Apply to a wide range of materials. Multiproperty measurement	Complex math analysis. Complex error analysis
Electron bombardment heat input	Solid and liquid metals. Nonmetals	330–3,200	50–400	2.0–10	High temperature coverage. Small specimen. AC techniques applicable	High vacuum; complex experimental apparatus
Monotonic heating	Ceramics, plastics, composites	4.2–3,000	50–400	2.0–12	Simple apparatus. Simple measurement. Wide temperature coverage	Inappropriate for good thermal conductors. Low precision
Photothermal methods	Small specimens of most solid material types	200–800	0.1–200	1.0–10	Test thermal diffusivity or thermal conductivity in appropriate models including NDT mode	Complex math analysis. Complex error analysis

Steady-state techniques typically include axial flow, radial flow, and guarded hot plate and hot-wire methods; while the most commonly used transient method is the laser flash method.

Axial Flow Methods

Axial flow methods have been long established with key measurement issues centered mainly on reduction of radial heat losses in the axial heat flow developed through the specimen from the electrical heater mounted at one end, in which the power dissipation of this heater is used in calculating column heat flux. These losses are minimal at low temperatures. As the specimen temperature moves above room temperature, control of heat losses becomes more and more difficult. Therefore, a great deal of attention centers on important experimental parameters such as the ratio of effective specimen conductance to lateral insulation conductance (the higher the better) and to the quality of guarding, which is the match of the axial gradient in the specimen to that of the surrounding insulation. In practice, cylindrical symmetry heat transfer is used. The subcategories can be divided into the following categories listed below (Anter 2007).

Absolute Axial Heat Flow

This method is mostly used in subambient environments. The system requires very precise knowledge of the electrical power feeding the heater, and the losses from the hot heater surfaces also play a major role.

Comparative Cut Bar (ASTM E1225 Test Method)

This is the most widely used method for axial thermal conductivity testing. The principle of the measurement is to have the heat flux pass through a known sample and an unknown sample and compare the respective thermal gradients, which will be inversely proportional to their thermal conductivities. Most commonly, the unknown sample is sandwiched between two known samples, the references, to further account for minor heat losses that are very difficult to eliminate, as shown in Figure 2.2. K_R is the thermal conductivity of the references. From this, the thermal conductivity of the unknown sample, K_s can be calculated as:

$$\frac{Q}{A} = K_s \frac{\Delta T_s}{L} = K_R \frac{\Delta T_1 + \Delta T_2}{2L}, \tag{2.4}$$

or

$$K_s = K_R \frac{\Delta T_1 + \Delta T_2}{2\Delta T_s}. \tag{2.5}$$

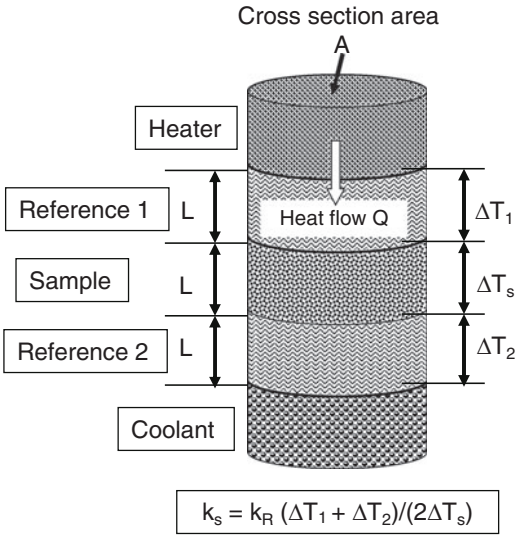

Fig. 2.2 Schematic of a comparative-guarded-axial heat flow system. The sample and two reference bars have the same height L and the same cross-section area A

Guarded or Unguarded Heat Flow Meter Method (ASTM C518, E1530 Test Methods)

A flux gauge is used, which is very similar in its purpose, to the references in the comparative cut bar method. In practice, the reference material has a very low thermal conductivity and, therefore, it can be made very thin. Usually, a large number of thermocouple pairs are located on both sides of the reference plate, connected differentially to yield directly an electrical signal proportional to the differential temperature across it. The assembly is cast into a protective coating for durability. This type of flux gauge is mostly used with instruments testing very low thermal conductivity samples, such as building insulations. In a similar fashion, flux gauges can be constructed from just about any material, thick or thin, depending on the material's thermal conductivity. Common requirements for all flux gauges are that the material used for the measuring section be stable, not affected by the thermal cycling, and the gauge be calibrated by some method independently. A very large variety of testing instruments use this method.

Guarded Hot Plate Method (ASTM C 177 Test Method)

The guarded hot plate is a widely used and versatile method for measuring the thermal conductivity of insulations. The specimens are often rather large. A flat, electrically heated metering section surrounded on all lateral sides by a guard heater section controlled through differential thermocouples, supplies the planar heat

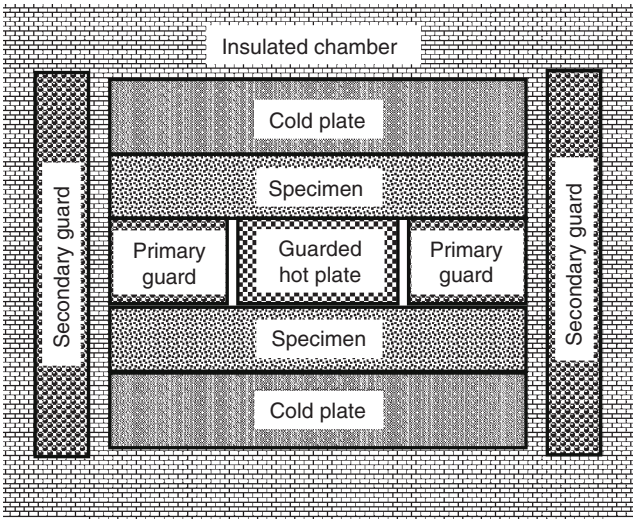

Fig. 2.3 Schematic of guarded hot plate method

source introduced over the hot face of the specimens. The most common measurement configuration is the conventional, symmetrically arranged guarded hot plate where the heater assembly is sandwiched between two specimens, as shown in Figure 2.3. In the single-sided configuration, the heat flow is passing through one specimen and the back of the main heater acts as a guard plane creating an adiabatic environment.

This is an absolute method of measurement and its applicability requires: (1) the establishment of steady-state conditions and (2) the measurement of the unidirectional heat flux in the metered region, the temperatures of the hot and cold surfaces, the thickness of the specimens and other parameters which may affect the unidirectional heat flux through the metered area of the specimen. Three different categories of measurement systems can be distinguished by an apparatus working around room temperatures, an apparatus working below room temperatures (down to about $-180°C$), and an apparatus working at high temperature (600°C or above). A given apparatus is most often best adopted for measurement in one of these temperature ranges.

Hot Wire Method (ASTM C1113 Test Method)

The hot wire method is a standard transient dynamic technique based on the measurement of the temperature rise in a defined distance from a linear heat source (hot wire) embedded in the test material. If the heat source is assumed to have a constant and uniform output along the length of test sample, the thermal conductivity can be derived directly from the resulting change in the temperature over

a known time interval. Hot wire methods are most commonly used to measure the thermal conductivity of refractory materials, such as insulating bricks and powder or fibrous materials. Because it is basically a transient radial flow technique, isotropic specimens are required. The technique has been used in a more limited way to measure properties of liquids and plastics materials of relatively low thermal conductivity.

The modification of this long-established technique is the probe method. The hot wire probe method utilizes the principle of the transient hot wire method. The heating wire as well as the temperature sensor (thermocouple) is encapsulated in a probe that electrically insulates the hot wire and the temperature sensor from the test material. This configuration is particularly practical where the specimen conductivity is determined from the response of a "hypodermic needle" probe inserted in the test specimen. Thus the method is conveniently applied to low-conductivity materials in powder or other semirigid form. A probe device can be used to measure the thermal properties of soils in situ, but most commonly a closely controlled furnace is used to contain the sample and produce the base temperatures for the tests. The probe contains a heater and a thermocouple attached to it. When a certain amount of current is passed through the heater for a short period of time, the temperature history of the heater's surface will take on a characteristic form. In the initial phase, the temperature will rapidly rise, and as the heat begins to soak in, the rate of rise becomes constant. When the thermal front reaches the outer boundary of the sample, the rise will slow down or stop altogether due to losses into the environment. From the straight portion of the rate curve (temperature vs. time) the thermal conductivity can be calculated.

Laser Flash Method

The laser flash method is the most common transient method for thermal diffusivity and conductivity measurement, which was developed by Parker, Butler, Jenkins, and Abbott of the U.S. Navy Radiological Defense Laboratory in 1961 (Parker et al. 1961). This method is based on depositing a very short but intense laser energy pulse on one surface of a disk-shaped sample, while monitoring the temperature excursion of the opposite face. From the characteristic time dependence of the temperature rise, called thermogram, thermal diffusivity can be calculated using Parker's formula (Parker et al. 1961; Gaal et al. 2004)

$$\alpha = \frac{138d^2}{t_{1/2}}, \tag{2.6}$$

where d is the sample's thickness and $t_{1/2}$ is the time necessary for the signal to reach 50% of its maximum value. The testing apparatus has been developed not only the basic technology concerning the homogenization of laser beam by the optical fiber system, the measurement of the transient temperature on the rear

surface of the specimen by high-speed infrared thermometer with a temperature scale, contact measurement at steady state temperature and the calculation of thermal diffusivity by the curve fitting method, but also the new technology of the differential laser flash calorimetry consists of a specimen holder which can hold two specimens (reference and measured) up to the high temperatures for simultaneous measurements of thermal diffusivity and specific heat capacity and a high-speed infrared thermometer which can simultaneously measure the temperature of the rear face of two specimens (Shinzato and Baba 2001).

Figure 2.4 shows a typical differential laser flash apparatus. The apparatus consists of a pulse laser, an optical fiber system with mode mixer as a pulse beam introduction unit, chamber with a sample support, a high-speed infrared thermometer (InSb elements, cooled by liquid nitrogen), differential amplifiers, and a transient memory. In addition, this apparatus is equipped with a beam profile monitor to provide the visual checking of the uniformity of a pulsed laser beam, and a vacuum pump, a circulating water-cooling unit and a personal computer for the analysis of measured data. An Nd-YAG laser (wavelength: 1.06 μm) is used as a pulsed laser and the half width of the laser pulse is selectable to either 300 or 500 μs mode with a switch. The output power of the laser can be changed up to 2 J for 300 μs mode and 5 J for 500 μs mode. The pulsed laser beam is focused into the optical fiber and homogenized in beam profile by the mode mixer and irradiated onto the specimens. The charging time required for one pulse shot is 30 s. The chamber can be operated in the range from room temperature to 1,800 K and the vacuum level of 0.05 Pa or lower to prevent oxidation and dirt proof and to suppress the heat loss caused by convection and can also be operated in an inert gas

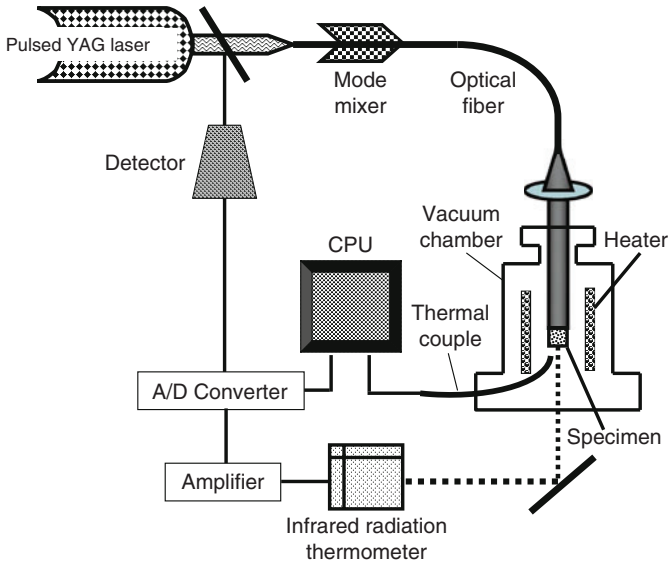

Fig. 2.4 Schematic of laser flash apparatus

atmosphere. The specimen is opaque and is a disk of 10 or 5 mm in diameter and from 0.5 to 3 mm in thickness, and black coating to absorb the laser beam is usually required for the specimen which is transparent, translucent, or low emissivity. The specimen with the diameter of 5 mm is used for the simultaneous measurements of thermal diffusivity and specific heat capacity. A high-speed infrared radiation thermometer equipped with five sensing elements has been developed and calibrated with a black body for the temperature scale. The precision of temperature calibration is $\pm$ 0.2 K. The temperature response of the infrared radiation thermometer is fast enough to respond the emitting signals, up to 10 kHz of infrared-emitting diode, without decrease of amplification factor or delay of phase (Shinzato and Baba 2001).

The advantages of the method originally was not only its speed (the actual test takes less than 1–2 s for most solids), but the ability to use very small, 5–12 mm diameter and 1–3 mm thick samples. This advantage became a problem for some composite materials, when such small samples are considered nonrepresentative of a larger body. However, the development of a system for large samples (30 mm diameter and up to 5 mm thickness) has alleviated this limitation to a great extent. Nevertheless, the need for specific heat capacity data remained the main limitation for this method in generating thermal conductivity data. While it was found that with careful experimental techniques, one could actually calibrate the response of the detector that generates the signal for the curve, the procedure itself imposed new limitations of its own. The process, simple in principle, involves testing a sample of known heat capacity first and then the unknown, and comparing the magnitude of the two resultant curves. Obviously, for such a differential computation the experimental variables (environment, electronics, energy pulse, etc.) must stay constant for both the sample and the reference. In reality this was and still is a serious problem for any instrument that can test only one sample at a time. It is easy to see that even the best case scenario (testing the reference over a temperature range, waiting for system to cool down, and then testing the unknown), will make close duplication of conditions nearly impossible. A major improvement has been achieved with multiple sample testing systems, where the unknown and the reference are tested side-by-side in true differential fashion. The results typically improved from the ± 7 to $\pm 10\%$ accurate data for single sample conventional systems, to ± 2 to $\pm 3\%$ for the multiple sample configurations. Because both specific heat capacity and thermal diffusivity are now measured in the same test, thermal conductivity is directly obtained in real time, with a priority knowledge of density (Gaal et al. 2004).

Coefficient of Thermal Expansion

The CTE is a basic physical property which can be of considerable importance in thermal managing design applications of a material. Materials usually expand as increase in temperature leads to greater thermal vibration of the atoms in the material, and hence to an increase in the average separation distance of adjacent

atoms. The linear CTE, α, designates how much a material will expand for each degree of temperature increase, as given by:

$$\alpha = \frac{\Delta L}{L_0}\Delta T, \tag{2.7}$$

where ΔL is the change in length of material in the direction being measured; L is original overall length of material in the direction being measured; ΔT is the change in temperature over which ΔL is measured. The magnitude of the CTE depends on the intermolecular or atomic bonding structure of the material. For example, strongly bonded structures such as ceramics have relatively low CTEs compared with metals, and loosely bonded structures such as polymers generally have high CTEs, especially those that are thermoplastics or elatomers.

Common methods for measuring CTE are shown in Table 2.2, including mechanical dilatometer, interferometry techniques, and thermomechanical analysis (Maglić et al. 1984). With typical CTEs in the range of 5–50 ppm/K, the changes in dimensions are extremely small and difficult to measure. Among these measuring methods, interferometry provides high accuracy, which looks at the changes in the interference pattern of monochromatic light, usually from a laser. With this technique it is possible to plot strain against temperature throughout a heating or cooling cycle. The slope of the strain/temperature curve at a given temperature is the instantaneous CTE. Furthermore, to give comparisons with earlier figures, the average slope over a temperature range can also be derived from the data.

Specific Heat Capacity

The specific heat capacity is another common physical property used to characterize the ability of the thermal managing materials to absorb heat. It is the amount of heat per unit mass required to raise the temperature by 1°C. The relationship between heat and temperature change is usually expressed by:

$$C = \frac{\Delta Q}{m\Delta T}, \tag{2.8}$$

Table 2.2 Thermal expansion measurement methods

Measurement method	Temperature range (°C)	Minimum coefficient of thermal expansion ($1.0e^{-6}$/K)	Accuracy (%)	Characteristics
Mechanical dilatometer	−150 to 2,000	Above 5	5.0–7.0	Medium precision
Interferometry techniques	−150 to 700	Below 5	1.0–3.0	High accuracy
Thermomechanical analysis	−120 to 600	Above 5	3.0–12	Inconsistent precision

Table 2.3 Specific heat measurement methods

Measurement method	Specimen materials	Temperature range (K)	Uncertainty (%)	Advantages	Disadvantages
Adiabatic	All	4–1,300	1.0–3.0	Very versatile. High sensitivity. Solid and liquid specimen applicable	Specimen in container. Limitation in high temperatures. Based on enthalpy data
Drop	All	300–2,000	1.0–3.0	Solid and liquid specimen	Specimen in container. Time consuming. Based on enthalpy data
Levitation	Electrical conductor (sphere)	1,000–2,500	2.0–5.0	Solid and liquid specimen	Specimen: electric conductor. Based on enthalpy data
Modulation	All	80–3,000	2.0–5.0	Multiproperty measurement	Limited to solid specimen
Pulse	Electrical conductor (wire, rod, tube)	1,000–7,000	2.0–10	Solid and liquid specimen applicable. Wide temperature coverage. Multiproperty measurement	Specimen: electric conductor. Complex instrumentation
Differential scanning	All	100–1,000	1.0–10	Fast and economical	Specimen in container. Limitation in high temperature

where C is specific heat in J/kg K, ΔQ is the heat energy put into or taken out of the material (J/mol), m is the mass of the material (kg), ΔT is the temperature differential (K). The relationship does not apply if a phase change is encountered, because the heat added or removed during a phase change does not change the temperature. There have been several methods developed, as shown in Table 2.3 (Maglić et al. 1984).

Thermal Shock Resistance

Thermal shock will cause cracking as a result of rapid temperature change. It usually occurs when a thermal gradient causes different parts of an electronic package to expand by different amounts. This differential expansion can be understood in terms of stress or strain, equivalently. At some point, this stress overcomes the strength of the material, causing a crack to form. If nothing stops this crack from propagating through the material, it will cause the electronic package to fail. The thermal shock resistance of a material can be expressed as (Krupke et al. 1986):

$$R = \frac{k\sigma(1-v)}{\alpha E}, \tag{2.9}$$

where k is the thermal conductivity, σ is maximal tension the material can resist, α is the thermal expansion coefficient, E is the Young's modulus, and v is the Poisson ratio. From (2.9), thermal shock can be prevented by: (1) reducing the thermal gradient of the electronic package by (a) changing its temperature more slowly and (b) increasing the material's thermal conductivity; (2) reducing the material's CTE; (3) increasing its strength; (4) increasing its toughness by (a) crack tip blunting, i.e., plasticity or phase transformation and (b) crack deflection.

The typical measuring methods are shown in Table 2.4. Among these methods, the impulse excitation technique has proved to be a useful tool. It can be used to measure Young's modulus, shear modulus, Poisson's ratio, and damping coefficient in a nondestructive way. The same test piece can be measured after different thermoshock cycles and in this way the deterioration in physical properties can be mapped out. The impulse excitation technique uses natural frequency, dimensions, and mass of a test piece to determine Young's modulus, Shear modulus, Poisson's ratio, and damping coefficient and then calculate the thermal shock resistance using (2.9). Dimensions and mass of a test piece can be easily measured.

Table 2.4 Thermal shock assessment methods

Heating method	Materials applicable	Advantages	Disadvantages
Induction (5–40 kW capacity)	Al, Cu, steels, Ni-superalloys	Rapid heating; complex sample geometries	Coil design experience; electric noise; high cost
Quartz lamp (radiation)	Ni, Co alloys; metallic composites	Inexpensive; uniform temperature; screening materials	Slow cooling rates; enforced cooling needed
Fluidized bed	Ni-based superalloys	Good for screening temperature fluidization resistance	Surface oxidation; need calculation of $\sigma - \varepsilon$ temperature transients
Flame burner heating	Ni-superalloys; steels	Screening of temperature fluidization resistance; surface corrosion representative of service	Oxidation; temperature transients
Dynamometer (friction heating)	0.5–0.7% C steels	Very high temperature on surface reached; representative of service	Oxides are wedged into cracks; friction changes with time
Impulse excitation	Materials that have enough stiffness to vibrate	Nondestructive; multiproperty measurement	Create vibration in a well prepared sample, and need a reference piece in some cases
Thermal cycling	Electronic packaging and thermal managing components and materials	Nondestructive; applicable a wide range of components and materials	Time consuming for some components and materials

Natural frequency is determined by gently tapping the test piece and analyzing the vibration. Tapping can be done using a small hammer or an automated tapping device. There are different ways to detect vibrations in the test piece: piezoelectric sensor, microphone, laser-vibrometer, accelerometer, etc. To optimize the results a microphone or a laser-vibrometer can be used because there is no contact between the test piece and the sensor. Laser-vibrometers are preferred to measure signals with extreme frequencies. These kinds of signals are usually only induced in very thin test pieces. Accuracy is determined by the quality of support of the test piece and the correctness of measurement of the dimensions and mass of the test piece. It is possible to do measurements within an accuracy rate of 0–1%. The best way to support a test piece is to use nylon fibers, but most systems use polyurethane foam strips as support. This makes it very difficult to measure small test pieces because the damping effect of the support is too big.

The most common method used for thermal shock testing is thermal cycling, which performed to determine the resistance of the part to sudden changes in temperature (JEDEC 2004). The parts undergo a specified number of cycles, which start at ambient temperature. The parts are then exposed to an extremely low (or high) temperature and, within a short period of time, exposed to an extremely high (or low) temperature, before going back to ambient temperature. Failure acceleration due to temperature cycling mainly depends on: (1) the difference between the high and low temperatures used; (2) the transfer time between the two temperatures; and (3) the dwell times at the extreme temperatures.

After the final cycle, external visual examination of the components or electronic packages should be performed under microscope. Electrical testing of the samples to device specifications also needs to be performed to detect electrical failures accelerated by the temperature cycle. For instance, for reliability testing or qualification of a electronic device or package, 1,000 temperature cycles are usually performed, with interim visual inspection and electrical test read points under microscope at a magnification of 200 and 500 times. Failure mechanisms accelerated by thermal shock include die cracking, package cracking, neck/heel/wire breaks, and bond lifting, etc.

Thermal Characterization of Micro/Nanomaterials

With developments of two-dimensional (2-D) (thin film) and 1-D micro- or nanostructured materials, many limits of bulk (3-D) material properties are being exceeded, i.e., the thermal conductivity of materials can be significantly improved or reduced depending on the system requirements. For instance, 1-D carbon nanotube (CNT) structures have very high thermal conductivity values. Conversely, thermoelectric thin films exhibit thermal conductivities which are lower than their bulk materials. This reduction in thermal conductivity is created by increased phonon interference and scattering caused by the introduction of low-dimensional structures. Typically 2-D structures are fabricated by depositing a repeating series

of thin films onto a thick bulk substrate. Determining the thermal conductivity of these thin films can be a challenge because of the small thickness of the films. The deposited film often cannot be removed from the substrate because the substrate provides mechanical support and interface adhesion strength for the film. Therefore, in experimental measurements, the substrate and the film must be measured together and then the properties of the substrate must be subtracted from the properties of the film/substrate composite. For measurements of thermal conductivity, if a steady state conduction method is used, errors can be introduced by the parasitic heat flow through the substrate and by radiation losses from the test sample. If the thermal conductivity of the substrate is relatively high, then the total heat flow through the substrate will be large compared with the heat flow through the film and subtraction of the substrate's contribution to heat conduction will significantly magnify measurement errors. If the thermal conductivity of the substrate is low, then radiation losses from the surface will dominate the heat flow through the test sample and the uncertainties of the radiative behavior will complicate the measurement of the thermal conductivity of the film when measurements are made at room temperature or above (Aller 2007).

Therefore, measuring the thermal conductivity of these micro- or nanostructured materials can prove challenging because of their small size and potentially large aspect ratios. The classic methods used for bulk material measurement would exceed their limitation. Hence, the 3ω method and thermoreflectance approach have been developed for measuring the thermal conductivity and specific heat of thin films and nanomaterials such as vertically grown CNTs, which would have increasing demand in thermal management of advanced electronic packaging.

The 3ω Method

The 3ω method is a transient method of accurately measuring the specific heat and thermal conductivity of a material. It uses a simple heater geometry, whose behavior can be solved from the heat diffusion equation. The heater is excited at a frequency of ω, this excitation produces temperature fluctuations in the material at a frequency of 2ω, and measurements of thermal conductivity and specific heat can be taken from the 3ω response. The heater is used simultaneously as a heater and a thermometer, therefore, no additional probes are required to carry out the method. The effect of black-body radiation produces less than 10% error in the measurement at 1,000 K and that this error was proportional to T^3, quickly becoming insignificant at lower temperatures (Aller 2007).

2-D Thin Films

The schematic illustration of a four pad measurement system of the 3ω method is shown in Figure 2.5. A thin metal band of width $2b$ ($10 < 2b < 100$ μm), and of length L ($L \approx 4$ mm), with four contacts, is prepared on the surface of the thin film

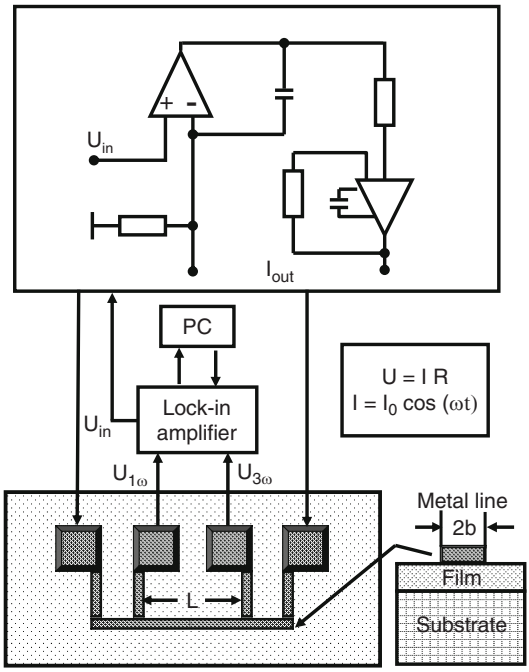

Fig. 2.5 Schematic illustration of four pad measurement system of the 3ω method

by photolithography. The resistance of the heater band is measured in function of the temperature by the four-wire method, so as to know the resistance between the two inside connections. The results are fitted with a linear model, in order to calculate the temperature coefficient of resistivity (Bourlon 2005)

$$\alpha_{\mathrm{R}} = \frac{1}{R}\frac{\mathrm{d}R}{\mathrm{d}T}. \tag{2.10}$$

The metal used for the heater is selected to have a temperature coefficient α_{R} as high as possible to increase the signal to noise ratio (S/N), such as gold or nickel. An alternating current

$$I(t) = I_0 \cos(\omega t), \tag{2.11}$$

where ω is the angular modulation frequency of the electric current, heats the metal band and the sample at an angular frequency 2ω by Joule effect. Because of the increase of the temperature of the heater band

$$\Delta T = \Delta T_0 \cos(2\omega t + \varphi), \tag{2.12}$$

the resistance R oscillates at the angular frequency 2ω and can be approximated as (Bourlon 2005)

$$R = R_0(1 + \alpha_R \Delta T) = R_0[1 + \alpha_R \Delta T_0 \cos(2\omega t + \varphi)]. \tag{2.13}$$

The amplitude ΔT_0 and the phase φ are directly linked to the thermal conductivity of the sample and to the angular frequency ω. The voltage V across the heater is obtained by Ohm's law (Bourlon 2005):

$$\begin{aligned} V(t) &= R(t)I(t) \\ &= R_0 I_0 \cos(\omega t) + \frac{1}{2} R_0 I_0 \alpha_R \Delta T_0 \cos(\omega t + \varphi) \\ &\quad + \frac{1}{2} R_0 I_0 \alpha_R \Delta T_0 \cos(3\omega t + \varphi). \end{aligned} \tag{2.14}$$

The first term, which is just the normal AC voltage at the drive frequency, does not contain any information on the amplitude ΔT_0 and the phase φ. The two other terms come from mixing the current at frequency ω with the resistance oscillations at 2ω. And as $R_\alpha \approx 3\ \mathrm{m\ K^{-1}}$ for the gold heater, and $\Delta T_0 \approx 1$ K, they are relatively small. The first of these terms is at the same frequency as the driving term. However, the last term appears at the third harmonic of the leading frequency, and for that reason it can be extracted from the total signal thank to a lock-in amplifier. The amplitude of this term is about 1% (Bourlon 2005)

$$V_{3\omega} = \frac{1}{2} R_0 I_0 \alpha_R \Delta T_0. \tag{2.15}$$

and its phase is φ.

For the 2-D heat conduction across a multilayer film-on-substrate system, the complex heater temperature rise can be expressed as (Bourlon 2005)

$$\Delta \tilde{T} = \Delta T_0 e^{i\varphi} \approx \frac{P_1}{\pi k_{y1}} \int_0^\infty \frac{1}{A_1 B_1} \frac{\sin^2(\lambda b)}{\lambda^2 b^2} d\lambda, \tag{2.16}$$

where

$$A_{i-1} = \frac{A_i \frac{k_{yi} B_i}{k_{y_{i-1}} B_{i-1}} - \tanh(\varphi_{i-1})}{1 - A_i \frac{k_{yi} B_i}{k_{y_{i-1}} B_{i-1}} - \tanh(\varphi_{i-1})}, \quad i = 2, \ldots, n, \tag{2.17}$$

$$\varphi_i = B_i d_i, \tag{2.18}$$

$$k_{xy} = \frac{k_x}{k_y}. \tag{2.19}$$

In the above expression, P_1 is the power per unit length (W/m), n is the total number of layers including the substrate; subscript i corresponds to the ith layer

starting from the top, subscript y corresponds to the direction perpendicular to the film/substrate interface (cross plane), b is the heater half width, k is the thermal conductivity of the layer, ω is the angular modulation frequency of the electric current, d is the layer thickness, and α is the thermal diffusivity. The effect of the thermal conductivity anisotropy is introduced through the term k_{xy}, which is the ratio of the in plane to cross plane thermal conductivity of the layer. For the substrate layer $i = n$, and if the substrate is semiinfinite $A_n = -1$. When the substrate has a finite thickness, the value A_n depends on the boundary condition at the bottom surface of the substrate: $A_n = -\tanh(B_n d_n)$ for an adiabatic boundary condition or $A_n = -1/\tanh(B_n d_n)$ if the isothermal boundary condition is considered.

For 2-D heat conduction across a thin film on semiinfinite substrate, if the heater band is deposed on an electrical insulating material, and if the heat flux is homogenous on all the width of the heat band, the complex heater temperature rise could be calculated by (Bourlon 2005)

$$\Delta\tilde{T} = \Delta T_s \approx \frac{P_l}{\pi k}\int_0^\infty \frac{\sin^2(\lambda b)}{\lambda^2 b^2\left(\lambda^2+q^2\right)^{1/2}}\mathrm{d}\lambda, \tag{2.20}$$

where $|1/q| = \sqrt{\alpha_s/2\omega}$ is the penetration depth of the thermal wave, α_s is the thermal diffusivity of the substrate.

For 2-D heat conduction across a thin film on a semiinfinite substrate, the temperature rise of the heater ΔT_0 is composed of two parts: the first, ΔT_s, is due to the substrate and the second, ΔT_F, is due to the thermal resistance of the thin film (Bourlon 2005).

$$\Delta T_0 = \Delta T_s + \Delta T_F. \tag{2.21}$$

If the width of heater is large compared with the thickness of the film, $b \gg d_F$, then the direction of the thermal flux is perpendicular to the film/heater interface; if the thermal conductivity of the thin film is smaller, then the thermal conductivity of the substrate, $k_F \ll k_s$; if the contact thermal resistances between the heater and the film and between the film and the substrate are negligible; and if the thermal diffusivity of the thin film, α_F, is important; then the temperature rise of the heater due to the thermal resistance of the thin film is (Bourlon 2005):

$$\Delta T_F = \frac{P_l d_F}{2bk_F}. \tag{2.22}$$

The precision of this measurement will depend on the precision of the measurements of the width of the heater band, $2b$, and of the thickness of the thin film, D_F, but also on the quality of the photolithography necessary to structure the heater. The measurement will be the more precise the bigger the difference of the thermal conductivity of the thin film and of the substrate.

1-D Nanomaterials

Taking a uniform rod- or filament-like specimen with four-probe configuration as for electrical resistance measurement, the two outside probes are used for feeding an electrical current, and the two inside ones for measuring the voltage across the specimen with the following conditions: (1) the specimen is suspended in a point between the two voltage probes to allow the temperature fluctuation; (2) all the probes are highly thermal-conductive, so the heat generated in the specimen can be dissipated into the substrate through the probes; (3) the specimen is maintained in a high vacuum and the whole setup is heat-shielded to the substrate temperature, so the radial heat loss through gas convection and radiation will be minimized. When an alternative electrical current of the form $I_0 \sin \omega$ passes through the specimen, the heat generation and transfer along the specimen will follow the partial differential equation (PDE) (Lu et al. 2001):

$$\rho C_p \frac{\partial}{\partial t} T(x,t) - \kappa \frac{\partial^2}{\partial x^2} T(x,t) = \frac{I_0^2 \sin^2 \omega t}{LS} [R + R'(T(x,t) - T_0)] \tag{2.23}$$

with boundary conditions $T(0,t) = T_0$, $T(L,t) = T_0$, $T(x,-\infty) = T_0$. Where C_p, k, R and ρ are the specific heat, thermal conductivity, electric resistance and mass density of the specimen at the substrate temperature T_0, respectively. $R' = (\mathrm{d}R/\mathrm{d}T)_{T_0}$. L is the length of the specimen between voltage contacts, and S is the cross section of the specimen. Through Fourier analysis, the 3ω voltage approximation can be derived as (Lu et al. 2001):

$$V_{3\omega,\mathrm{rms}}(t) \approx \frac{4 I_{\mathrm{rms}}^3 L R R'}{\pi^4 k S \sqrt{1 + (2\omega\gamma)^2}}, \tag{2.24}$$

where $\gamma = (L^2/\pi^2\alpha)$ is the specimen's characteristic thermal time constant in axial direction; $\lambda = \sqrt{\alpha/2\omega}$ is thermal wavelength; and $\alpha = (k/\rho C_p)$ is thermal diffusivity.

For a CNT specimen, when $L = 0.9$ μm, $S = 1.25\mathrm{e}^{-16}$, $I_0 = 1.41$ μA, $R = 3$ kΩ, $R' = 140$ Ω/K, $k = 1$–$1{,}000$ W/m K, $\rho = 1$ kg/m^3, $C_p = 1$–$1{,}000$ J/kg K, the operational limits would be $(I_0^2 R' L/n^2\pi^2 kS) \ll 1$ ($2.0\mathrm{e}^{-4}$ for $k_{\max}$; and 0.2 for $k_{\min}$); $\alpha = (k/\rho C_p) = 1{,}000\,\mathrm{m}^2/\mathrm{s}(\max)$ or $1\mathrm{e}^{-3}$ m^2/s; and $\lambda(1\,\mathrm{kHz}) = \sqrt{\alpha/2\omega} = 0.28\,\mathrm{m}$ (max) or $2.8\,\mathrm{e}^{-4}$m (min). As $\lambda \gg L$, (2.24) can be expressed as

$$V_{3\omega,\mathrm{rms}} \approx \frac{4 I_{\mathrm{rms}}^3 L R R'}{\pi^4 k S}. \tag{2.25}$$

Thermoreflectance Approach

The basic principle of the transient thermal reflectance (TTR) method is to heat a sample by laser irradiation and probe the changes in the surface reflectivity of the

heated material. The source of energy in the TTR method is normally provided by a pulsed laser with short pulse duration. During each pulse, a given volume below the sample surface heats up due to the absorbed laser light energy. The depth of the volumetric heating is determined by the optical penetration depth, which is a function of laser wavelength and surface material properties. After each laser pulse, the sample cools down to the initial ambient temperature. During this process, a probing CW (continuous wave) laser light reflected from the sample surface at the heating spot center is collected on a photodetector (1 ns maximum rise time) that reads the instantaneous surface reflectivity (Kim 2007).

The TTR method is typically used for the measurement of thin film through-plane thermal conductivity or interface thermal resistivity. The TTR system uses the fact that the relative change in the temperature of the surface material is linearly proportional with the relative change in the reflectivity within a wide but finite temperature range (Kim 2007):

$$\frac{\Delta T}{T} = \frac{\Delta R}{R}, \tag{2.26}$$

where T is the temperature and R is the reflectivity of the materials. The changes in surface reflectivity, are then recorded by an oscilloscope (at rates of up to 5 Giga-samples per second). The result of the experiment is a transient normalized temperature response, which represents the overall heat transfer behavior of the layers of materials including the unknown material under test. To extract the thermal conductivity from the recorded temperature response, an identical mathematical representation of the corresponding physical measurement problem is solved numerically with guessed thermal properties with the intention of matching the experimental and numerical transient normalized temperature responses. A mathematical optimization technique makes it possible to systematically vary the desired unknown properties and compare each resulting numerically obtained response to the reference experimental data until the error between them is minimized in the root-mean-square sense. The final numerical solution, therefore, yields the desired unknown parameters, which represent the best fit to the actual thermal properties of the physical sample. By using a two-parameter optimization technique, the method can yield the thermal conductivity of the material under test and the interface resistance between this material and the absorption layer on top of it. The transient heat transfer in the TTR method can be described by the use of the heat equation, as follows (Kim 2007):

$$\rho C_p \left(\frac{\partial T}{\partial t}\right) = \nabla(K \nabla T) + \dot{Q}_{\text{ab}}, \tag{2.27}$$

where ρ is the mass density of the material, C_p is its specific heat, t is the time, K is its thermal conductivity, and $\dot{Q}_{\text{ab}}$ is the heat source created by absorption of the laser light energy. Moreover, the heat transfer inside the sample under test is governed by the 2-D heat equation in polar coordinates and can be written as follows:

$$\frac{\partial T}{\partial t} = \alpha(T)\left(\frac{\partial^2 T}{\partial r^2} + \frac{1}{r}\frac{\partial T}{\partial r} + \frac{\partial^2 T}{\partial z^2}\right) + \frac{1}{\rho C_p}\dot{Q}(r,z,t), \tag{2.28}$$

where r and z are dimensionless coordinates and α is the thermal diffusivity of the material, which is $\alpha = K/(\rho C_p)$. The heat source $\dot{Q}(r,z,t)$, can be expressed as (Kim 2007):

$$\dot{Q}(r,z,t) = I(t)(1-R)\gamma e^{-\gamma z}, \tag{2.29}$$

where γ is the absorption coefficient of the top layer, and $I(t)$ is a Gaussian temporal distribution as follows (Kim 2007):

$$I(t) = \frac{2F}{\tau\sqrt{\pi}} e^{-4\left(\frac{t-t_0}{\tau}\right)^2}, \tag{2.30}$$

where F is the fluence of laser irradiation, τ is the duration of the heating laser pulse which is 6.1 ns, and $t_0 = 7$ ns is the time at which the intensity reaches its maximum value. When the dimension of the probing spot is close to two orders of magnitude smaller than the heating laser spot, the heated sample under test can be treated as a semiinfinite solid for the 1-D problem. The diameter of the heated spot (YAG Laser) is 185 μm, for example, while the probing spot is around 2.5 μm, which is small enough to make $(\partial T/\partial r) \approx 0$ in the probing spot area. Thus the 1-D heat equation can be induced from 2-D equation. Thus, the 1-D heat equation is induced from the 2-D (2.28) as follows (Kim 2007):

$$\frac{\partial T}{\partial t} = \alpha\left(\frac{\partial^2 T}{\partial z^2}\right) + \frac{1}{\rho C_p}\dot{Q}_{\text{ab}}(r,z,t). \tag{2.31}$$

The first boundary condition is an adiabatic boundary condition at the top of the sample as $\partial T/\partial t = 0$, at $z = 0$ because the time scale of the TTR is in the nanosecond range, natural convection and conduction from the sample to the surrounding medium (air) can be neglected. The second boundary condition is an isothermal boundary condition at the bottom of the sample as $T = T_{\text{chuck}}$, at $z = \infty$ because the sample is located on a thermochuck that keeps the temperature constant at T_{chuck}. Initially, because the materials are at ambient temperature, the initial condition is written as $T = T_{\text{ambient}}$, at $t = 0$. During the heating and cooling process, the instantaneous surface reflectivity is acquired by the probing CW laser light reflected from the sample surface at the center of the heated spot, and then the thermal diffusivity of the material is extracted by solving the 1-D inverse heat (2.31) based on (2.26). This would be accomplished by first numerically simulating the transient heating caused by the laser pulse and then fitting the experimental results with the computed data in the TTR system (Kim 2007).

Electrical Properties and Measurement Techniques

Electrical Conductivity and Resistivity

Electrical conductivity or resistivity is key physical property of all thermal managing materials. Electrical conductivity, k, is a measure of how well a material accommodates the movement of an electric charge. It is the ratio of the current density, J (A/m^2), to the electric field strength, E (V/m).

$$k = \mathbf{J}/\mathbf{E}. \tag{2.32}$$

Its SI (International System of Units) derived unit is the S/m (Siemens per meter), but conductivity values are often reported as percent IACS (International Annealed Copper Standard). The conductivity of the annealed copper (5.8108×10^7 S/m) is defined to be 100% IACS at 20°C, adopted since 1913. Electrical resistivity, ρ (Ω m), is the reciprocal of conductivity. It is the opposition of a body or substance to the flow of electrical current through it, resulting in a change of electrical energy into heat, light, or other forms of energy. The amount of resistance depends on the type of material and the applied magnetic field.

The resistivity of any material varies with temperature. For instance, the resistivity of metals usually increases as temperature increases, while the resistivity of semiconductors usually decreases as temperature increases. For temperature range that is not too great, this variation can be represented approximately as a linear relation:

$$R_T = R_0[1 + \alpha(T - T_0)], \tag{2.33}$$

where R_T and R_0 are the values of the resistance at temperature T and T_0, respectively. T_0 is often taken to be either room temperature or 0°C. α is the temperature coefficient of resistivity. Pure metals have a small, positive value of α, which means that their resistance increases with increasing temperature. There are materials in which resistance decreases with increasing temperature. A thermistor is an example of such a material. It is made of semiconductors, such as oxides of manganese, nickel and cobalt mixed in the desired proportion with a binder and pressed into shape. Thermistors are very sensitive to even small changes of temperature, therefore they are often used as thermometers. The change of resistance of a thermistor caused by temperature change is a nonlinear function and can be approximated by the following formula:

$$R_T = R_0 \exp[\beta(1/T - 1/T_0)], \tag{2.34}$$

where R_T and R_0 are the resistance values at absolute temperatures T and T_0 (K), β (K) is a constant over a limited temperature range and characterizes a property of material. Some materials have very complicated temperature dependencies of

resistance. For example, nichrome wire, used as a heating element in most space heaters, practically does not change its resistance in the temperature range between 0 and 100°C. For other materials, such as carbon resistors, the resistance may be constant for a narrow temperature range and show a large effect beyond that range.

The measuring methods for electrical conductivity mainly include eddy current testing, two-point technique, four-point technique, and van der Pauw technique.

Eddy Current Testing

Eddy current testing uses electromagnetic induction for conducting examinations. When alternating current is applied to the conductor, a testing probe, or sensor, a magnetic field develops in and around the conductor. This magnetic field expands as the alternating current rises to maximum and collapses as the current is reduced to zero. If another electrical conductor, testing sample, is brought into the close proximity to this changing magnetic field, current will be induced in this second conductor, which is measured and correlated with the conductivity of the testing sample.

The testing for electrical conductivity is usually to null an absolute probe in air and place it in contact with the sample surface. And this technique is generally limited to nonmagnetic materials, as the change in impedance of the coil probe can be correlated directly to the conductivity of the material. Because conductivity changes with temperature, the measurements should be made at a constant temperature and adjustments made for temperature variations when necessary. The thickness of the specimen should generally be greater than three standard depths of penetration. This is so the eddy currents at the back surface of the sample are sufficiently weaker than the variations in the specimen thickness that are not seen in the measurements.

Except electrical conductivity measurement, eddy current testing as a nondestructive test tool can also be used for crack detection, material thickness measurements, coating thickness measurements, as well as conductivity measurements for material identification; heat damage detection, case depth determination, and heat treatment monitoring. The major advantage of this method is that it can be used for measuring complex shapes and wide size ranges of conductive materials with various defects. The main limitations of eddy current testing method include: (1) only conductive materials can be inspected; (2) sample surface must be accessible to the probe, and surface finish or roughness may interfere testing result; (3) depth of signal penetration is limited; and (4) flaws such as delaminations that lie parallel to the probe coil winding and probe scan direction are undetectable.

Two-Point Technique

The resistivity of a material can be obtained by measuring the resistance and physical dimensions of a bar of material. The material is cut into the shape of a rectangular bar

of length l, height h, and width w. Copper wires are attached to both ends of the bar. A voltage source applies a voltage V across the bar, causing a current I to flow through the bar. The amount of current I that flows through the bar is measured by the ammeter, which is connected in series with the bar and voltage source. The voltage drop across the ammeter should be negligible. The resistance R of the bar is given by $R = V/I$, where R = resistance in Ω; V = voltage in volts, I = current in amps. The two-point resistivity of the material can be obtained by (Heaney 1999):

$$\rho = (Rwh)/l, \tag{2.35}$$

where ρ is the resistivity in Ω m, R is the measured resistance in Ω, and w, h, and l are the measured physical dimensions of the sample bar in meters. In practice, measuring resistivity with a two-point technique is often not reliable, because of some resistance between the contact wires and the material, or in the measuring equipment itself. These additional resistances make the resistivity of the material measure higher than it really is.

Four-Point Technique

Four-point measurement technique on a bar of material uses four wires attached to the sample bar. A current source forces a constant current through the ends of the sample bar. A separate ammeter measures the amount of current I passing through the bar. A voltmeter simultaneously measures the voltage V produced across the inner part of the bar. The four-point resistivity of the material can then be expressed as (Heaney 1999):

$$\rho = (Vwh)/(Is), \tag{2.36}$$

where ρ = resistivity in Ω m, V = voltage measured by the voltmeter in volts, w = width of the sample bar measured in meters, h = height of the sample bar measured in meters, I = current the ammeter measures flowing through the sample in amperes, s = distance between the two points where the voltmeter wires make contact to the bar, measured in meters.

Van der Pauw Technique

The four-point measurement technique described earlier has assumed the material sample has the shape of a rectangular thin film or a bar. There is a more general four-point resistivity measurement technique that allows measurements on samples of arbitrary shape, with no need to measure all the physical dimensions of the sample. This is the van der Pauw technique. There are four conditions that must be satisfied to use this technique (Heaney 1999): (1) the sample must have a flat shape of uniform thickness; (2) the sample must not have any isolated holes; (3) the

sample must be homogeneous and isotropic; (4) all four contacts must be located at the edges of the sample.

In addition to these four conditions, the area of contact of any individual contact should be at least an order of magnitude smaller than the area of the entire sample. For small samples, this might not be possible or practical. If sufficiently small contacts are not achievable, it is still possible to do accurate van der Pauw resistivity measurements, using geometric correction factors to account for the finite size of the contacts.

Permittivity and Its Characterization

Permittivity, ε, also called electric permittivity or dielectric constant, is a constant of proportionality that exists between electric displacement (D) and electric field intensity (E): $D = \varepsilon\,\mathrm{E}$. The vacuum permittivity $\varepsilon_0 = 1/(c^2\mu_0) \approx 8.85 \times 10^{-12}$ farad per meter (F/m), where c is the speed of light; μ_0 is the permeability of vacuum. The linear permittivity of a homogeneous material is usually given relative to that of vacuum, as a relative permittivity $\varepsilon_\mathrm{r} = \varepsilon/\varepsilon_0$. When ε_r is greater than 1, these substances are generally called dielectric materials, or dielectrics, such as various ceramics, plastics, and certain metal oxides. A high permittivity tends to reduce any electric field present. For instance, the capacitance of a capacitor can be increased by increasing the permittivity of the dielectric material. Common methods used for the measurement of permittivity include loaded resonant waveguide cavity, open ended coaxial line, and loaded coaxial transmission line. Loaded resonant waveguide cavity methods offer the good measurement accuracy, particularly for measurement of imaginary part of the permittivity for determining the energy losses in a material. The sample material is mounted inside a resonant cavity to fit well with certain dimensions and thereby loading the cavity. This method only covers a narrow frequency band to maintain the resonance status of a cavity. However, this can be improved to some extend by including higher order resonant modes.

The open ended coaxial line is a nondestructive test method. The coaxial probe is pressed against a test sample to measure the reflection coefficient. And then the permittivity can be determined from the reflection coefficient. Because this method is sensitive to air gaps that disturb the electric field, the probe and the sample, its measurement accuracy is not as good as the other two methods (Tong 2009).

In the loaded coaxial transmission line method the material under test is placed to fill the volume between the inner and outer conductor in a section along the transmission line. The dimensions of the sample piece are critical to ensure a precise fit. The material may load the line and cause a change of characteristic impedance. Both reflection and transmission through the fixture is used when calculating the test material data. The measurement accuracy of this method is not as good as that of loaded cavity resonance measurement methods. An advantage

of the loaded coaxial transmission line method is that it offers the possibility to perform measurements in a broad frequency band (Tong 2009).

The selection of the measurement method to use depends on restrictions on sample preparation and desired frequency range and accuracy of the data. The loaded cavity resonance measurement method gives high accuracy data for narrow-band measurements at frequencies of over 100 GHz. The open ended coaxial line offers a method where only a flat surface of sample material is needed. The loaded coaxial transmission line method makes it possible to measure over wide frequency range with better accuracy than what the open ended coaxial line method offers (Tong 2009).

Thermomechanical Characterization

To produce low cost and compact electronics goods, high input/output surface mounted chip carriers on printed circuit boards (PCBs) or printed wire boards, such as multilayer PCBs, flip chip, flip-chip with underfill, chip scale package, and ball grid array packages, have been widely used in electronic packaging assemblies. One critical reliability concern about this type of electronic packaging is the thermomechanical stress and strains induced by temperature change. For example, the in-plane strain affects the thermal fatigue life of surface mount solder interconnections, while the out-of-plane strain affects the mechanical integrity of the plated-through holes of the PCBs. The primary causes for this strain are thermal mismatch in properties among constituent materials of the package as well as mechanically induced flexure. A variety of techniques have been used to characterize the stress and strain in the electronic packaging. For instance, a micromechanical test apparatus was developed for use with a compact four-beam moiré interferometer. The interferometer was used to evaluate whole field displacements of plastic ball grid array packages over a range of temperatures and under four-point bending.

In fact, thermomechanical failure has become one of major concerns for electronic packaging design, especially because the high degree of integration, speed, and power level and the high cost of production have imposed more stringent reliability requirements on individual components. Therefore, a fully understanding of thermomechanics of component materials is very important as they apply to electronic packaging. Thermal stress effects can be evaluated by experimental validation, matched with simulation by coupling a heat transfer analysis (steady-state or transient) and a structural analysis (static stress with linear or nonlinear material models or mechanical event simulation).

This section will introduce basic concepts of thermally induced stress, strain, and materials behavior characterization methods, as well as the finite-element method and its application to thermomechanical analysis, and various failure theories, including fatigue and fracture with analytical solutions, which provide insight into the behavior of layered assemblies of electronic packaging and thermal cooling system.

Characterization Techniques of Thermally Induced Stress and Strain

As shown in Figure 2.6, stress is defined as force per unit area, which can be interpreted as internal tractions that act on a defined internal datum plane within a solid. Depending on its action direction, it can usually be divided into normal stress and shear stress. Strain is defined as the amount of deformation an object experiences compared with its original size and shape under the action of stress. Stress components acting perpendicular to the surfaces are called normal stresses; stress components acting along planes are referred as shear stresses. In the static case, when all forces acting on three orthogonal faces of a body are in equilibrium, the matrix of nine stress components in a Cartesian coordinate system is called stress tensor.

The strain tensor, ε, is a symmetric tensor used to quantify the strain of an object undergoing a small 3-D deformation: the diagonal coefficients ε_{ii} are the relative change in length in the direction of the i direction (along the x_i-axis); the other terms $\varepsilon_{ij} = 1/2\gamma_{ij}$ $(i \neq j)$ are the shear strains, i.e., half the variation of the right angle (assuming a small cube of matter before deformation). The deformation of an object is defined by a tensor field, i.e., this strain tensor is defined for every point of

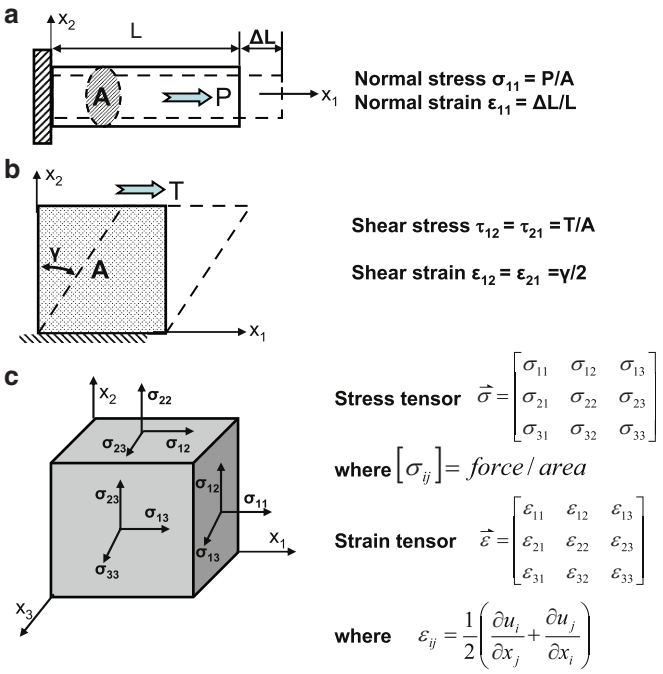

Fig. 2.6 Schematic of concept of stress and strain. (**a**) Normal stress and strain in 1-D system; (**b**) shear stress and strain in 1-D system; (**c**) stress and strain tensors in 3-D system

the object. This field is linked to the field of the stress tensor by the generalized Hooke's law.

In case of small deformations, the strain tensor is the linearized Green strain tensor or Cauchy's infinitesimal strain tensor, defined by the equation:

$$\varepsilon_{ij} = \frac{1}{2}\left(\frac{\partial u_i}{\partial x_j} + \frac{\partial u_j}{\partial x_i}\right),$$

where u represents the displacement field of the object's configuration (i.e., the difference between the object's configuration and its natural state). This is the symmetric part of the Jacobian matrix. The antisymmetric part is called the small rotation tensor (Symon 1971).

In the electronic packaging, changes in temperatures causes thermal effects on materials. Some of these thermal effects include thermal stress, strain, and deformation. Thermal deformation means that as the thermal energy (and temperature) of a material increases, so does the vibration of its atoms/molecules; and this increased vibration results in what can be considered a stretching of the molecular bonds–which causes the material to expand. Of course, if the thermal energy (and temperature) of a material decreases, the material will shrink or contract. The thermal strain, which results from unrestrained expansion due to temperature change, ΔT, is given by $\varepsilon_1 = \varepsilon_2 = \varepsilon_3 = \alpha(T)\Delta T$, where $\alpha(T)$ is the CTE, T is the temperature, and ΔT is the temperature change. For many materials, α is not a strong function of the temperature and can be treated as a constant over a reasonably large variation in temperature.

In electronic packaging including the thermal management system, the main objectives of the stress–strain analysis are to determine the causes of failure, to conduct design optimizations and predict reliabilities. Because most of the current prediction theories and models use thermomechanical stresses and strains as parameters for estimating damages and failures, accurate determinations of strains and stresses are indispensable in the reliability analysis and predictions. In order to obtain critical strains and stresses in the package structures, several methods have been developed, such as micromechanical tester, moiré interferometry, and speckle techniques.

Micromechanical Tester

The micromechanical tester or diamond indenter is usually used to evaluate the mechanical response of a small volume of material near the surface of a sample by probing the surface with a diamond indenter of known geometry. A piezoelectric transducer drives the indenter into the sample surface while load, depth of penetration, and displacement data are continuously collected. There are several diamond indenters, such as Vickers (square pyramid), Knoop (elongated square pyramid), Berkovich (triangular pyramid), and right circular cones with tip radii of 1, 5, 10, and 50 μm. A

PC (personal computer) interface is used to control the machine and collect data. The micromechanical tester is generally equipped with a hot stage: fixed temperatures from ambient to 100°C; and a tangential load cell for measuring lateral forces.

The micromechanical tester can be used to characterize the mechanical properties and adhesion strength of films. Indentation, microscratch, load relaxation, indentation fatigue, indentation creep, and dynamic mechanical experiments can be performed on coatings to obtain information on hardness, elastic modulus, storage and loss moduli, friction coefficients, film adhesion, and fracture toughness. Three- and four-point bending, tensile, compression, crush, peel, and fiber pushout tests can also be performed.

Scratch tests are performed by drawing the indenter across the surface as it penetrates. Delamination of films allows qualitative and, in some cases, quantitative evaluation of interfacial properties.

Virtually any test that requires pushing or pulling under carefully controlled conditions within the physical limits of the micromechanical tester can be performed. The micromechanical tester can be used for testing materials and coatings of all kinds from highly viscous polymers to diamond-like carbon. Maximum sample size: specimens 2 cm high and 5 cm across. Larger samples can be accommodated with some geometrical constraints. A smooth surface produces best results. Load resolution: 50 μN; depth resolution: 5 nm.

Moiré Interferometry

Moiré interferometry is a whole-field optical interference technique with high resolution and high sensitivity for measuring the in-plane displacement and strain fields. This method has been successfully used to measure the thermomechanical deformations of electronic packages with the objective to study package reliability.

Moiré interferometry relies upon the interference of laser light to produce maps of displacement. Interference occurs through the superposition of the electric field vectors of rays of light, with the same frequency, meeting at a point in space. Depending on both the amplitudes and difference in phase between superimposed rays of light, the resulting intensity for two interfering light rays is described by (Stout 1994):

$$I = a_1^2 + a_2^2 + 2a_1a_2 \cos \Phi, \tag{2.37}$$

where a_1 = the electric field amplitude of beam 1, a_2 = the electric field amplitude of beam 2, Φ = the phase difference between beams 1 and 2. When two interfering light rays have equal amplitudes, (2.34) simplifies to

$$I = 4a^2 \cos^2\left(\frac{\Phi}{2}\right), \tag{2.38}$$

where $a = a_1 = a_2 =$ the electric field amplitude of both beams. If both beams are out of phase by π radians, completely destructive interference occurs.

During measurement in an interferometer, a high frequency diffraction grating is transferred on to the testing area of a specimen. The optical arrangement in the moiré interferometer produce a virtual reference grating of spatial frequency f by means of the interference of two coherent beams (beam 1 and beam 2) from a laser light source. The virtual reference grating is superimposed on the specimen grating to form a fringe pattern, which is a displacement contour map. Each fringe passes through points with the same displacement in the electrical field corresponding to the x and y direction. Fringes are numbered consecutively, with fringe order N_x and N_y. The formulas for determining the displacements at each point in the field from the fringe orders can be written as (Post and Han 2009):

$$U = \frac{1}{f} N_x; \quad V = \frac{1}{f} N_y, \tag{2.39}$$

where U and V are displacements in the x- and y-directions, respectively. For the strains at each point

$$\varepsilon_x = \frac{\partial U}{\partial x} = \frac{1}{f}\left(\frac{\partial N_x}{\partial x}\right), \tag{2.40}$$

$$\varepsilon_y = \frac{\partial V}{\partial y} = \frac{1}{f}\left(\frac{\partial N_y}{\partial y}\right), \tag{2.41}$$

$$\gamma_{xy} = \frac{\partial U}{\partial y} + \frac{\partial V}{\partial x} = \frac{1}{f}\left(\frac{\partial N_x}{\partial y} + \frac{\partial N_y}{\partial x}\right), \tag{2.42}$$

where ε and γ are normal and shear strains, respectively. Thus, the strains are determined by the rate of change of fringe orders in the patterns, or the fringe gradient surrounding each point. Stresses are determined from the strains, using the stress–strain relationships (or the constitutive equations) for the specimen material.

Moiré measurements are performed routinely in the interferometric domain with fringes representing subwavelength displacements per contour. Since moiré responds only to geometric changes, it is equally effective for elastic, viscoelastic, and plastic deformations, for isotropic, orthotropic, and anisotropic materials, and for mechanical, thermal, and dynamic loadings (Post and Han 2009). Moiré interferometry can be used to contour surfaces at any wavelength longer than 10 μm (with difficulty) or 100 μm with reduced environmental requirements and no intermediate photographic recording setup. For nondestructive testing, holographic interferometry has a precision of a small fraction of a micrometer and is useful over a deformation amplitude of a few micrometers, whereas moiré interferometry has a precision ranging from 10 to 100 μm to mm, with a correspondingly increased useful range of deformation amplitude. A widely used moiré interferometer in

electronic package analysis is the Portable Engineering Moiré Interferometer originated from IBM. It uses a grating frequency of 1,200 lines/mm, which yields a spacing of the interference fringe corresponding to 417 nm of in-plane displacement. The sensitivity is adequate for measuring the overall thermal deformation of electronic packages. However, it is not sufficient for measuring thermal deformation in high-density electronic packages, particularly for small features, such as solder balls. Such measurement can be performed using phase-shifting moiré interferometry or speckle techniques.

Speckle Techniques

The speckle pattern is formed by the self-interference of a large number of random coherent waves scattered from a rough object surface or propagated through a medium of random refractive index fluctuations. The remarkably simple and effective way to use the speckle effect in the measurement of displacement and deformation is speckle photography and speckle interferometry. They can give point-by-point or whole-field data, and the level of sensitivity can be adjusted. Speckle interferometry is based on the coherent addition of scattered light from an object surface with a reference beam that may be a smooth wave front or a scattered field from a reference object or from the sample. Compared with the speckle photography method, speckle interferometry is more sensitive (An 2002).

Laser speckles is a phenomenon that is experienced if an optically rough surface is illuminated by a highly coherent laser source. They are formed by the interference of dephased but coherent wavelets, emanating from different microscopic elements of the specimen's surface and cause a randomly looking pattern. This speckle pattern is characteristic for a particular surface element just like a fingerprint and if that surface element is undergoing a pure displacement δ_{surf}, the associated speckles, as recorded by a camera at a fixed location, are displaced likewise by δ_{image} image. If the specimen, in addition to pure displacement, is also strained, the associated structural changes of the speckles will for most applications cause a negligible additional speckle-displacement. The usual digital image-processing algorithm, is used to track speckles, based on pattern matching by some kind of correlation algorithm, which usually gives displacement values that are integer multiples of a quant (usually the size of the pixel pitch of the camera; Zimprich and Zagar 2007).

The electronic image acquisition and computer image processing has been applied to the speckle metrology and lead to a versatile method called electronic speckle pattern interferometry (ESPI), television holography, or electrooptic holography. The advances in the development of CCD (charge-coupled device) cameras and computer-based image processing have propelled ESPI to the forefront of thermomechanical analysis of electronic packaging. The attractiveness and versatility of speckle metrology lies in its ability to measure (An 2002): (1) deformation or displacement with variable sensitivity to in-plane and out-of-plane direction; (2) 3-D object shape surface roughness; (3) vibration.

ESPI has been applied for noncontact, real-time evaluation of thermal deformation in a flip-chip package. The spatial resolution of ESPI was increased to submicron scale by magnifying the areas studied in order to measure the deformation of such small-scale components as the solder in the flip-chip package. Thermal deformation in the horizontal and vertical directions around the solder joints, for instance, was measured as 2-D mappings during heating from 25 to 125°C. ESPI was successful in obtaining information on the complicated deformation field around the solder joints. Furthermore, the shear strain could also be calculated using the measured thermal deformation around each solder joint. The applicability of ESPI to flip-chip packages could be verified by comparing the ESPI results with those of finite-element analysis (FEA).

Fundamental Equations of Deformable Bodies

Deformation analysis of electronic system is usually based on continuum mechanics using mathematical techniques and physical laws of statics, kinematics, and dynamics. Statics deals with the equilibrium of forces acting on a body at rest or moving with constant velocity. Dynamics deals with bodies in motion, which is divided into kinematics and kinetics. Kinematics is concerned only with the geometry of motion. It is the study of the positions, angles, velocities, and accelerations of body segments and joints during the motion. Kinetics is concerned with the force analysis of bodies in motion (Szostak-Chrzanowski et al. 2006). The basic conditions and relations of continuum mechanics involve equations of equilibrium, strain displacement equations, constitutive equations, and boundary conditions.

The conditions of equilibrium are fundamental equations of continuum mechanics. The acting forces on the object must be in equilibrium. The forces acting on the object are divided into external forces acting on boundaries and body forces. An acting force F per unit area A is defined as a stress σ. If σ_{ij} denotes stress tensor and the stress tensor is symmetric, that is, $\sigma_{ij} = \sigma_{ji}$, the equation of equilibrium is (Szostak-Chrzanowski et al. 2006)

$$\sigma_{ij} \mathrm{d}A_i = \mathrm{d}P_j. \tag{2.43}$$

Eigenvalues of the stress tensor are known as principal stresses. The principal stress directions are the eigenvectors of the stress tensor. In case of a body in motion, the motion is described by dynamic equations. For small motions, the velocity is a partial derivative of displacement function U and is given as (Szostak-Chrzanowski et al. 2006):

$$U_i' = \frac{\partial U_i}{\partial t}. \tag{2.44}$$

Negative product of acceleration and mass density ρ, known as d'Alambert inertia force per unit volume, is added to the acting force F_i. This gives the dynamic equation using Newton's law in the form (Szostak-Chrzanowski et al. 2006):

$$\sigma_{ij} \mathrm{d}A_i = -\mathrm{d}F_i + \mathrm{d}(\rho U'_i). \tag{2.45}$$

The kinematic relations are between strain and displacement and relate to the geometry of the motion which leads from undeformed to deformed position. The kinematic relations are independent of acting forces and type of material behavior (elastic or inelastic). The strain tensor is denoted as ε_{ji} and has nine components in the 3-D space. In case when displacements U are small it means, $U_{i,j} = \partial U_i / \partial x_j \ll 1$, the strain tensor components are (Szostak-Chrzanowski et al. 2006)

$$\varepsilon_{i,j} = \frac{1}{2}(U_{i,j} + U_{j,i}). \tag{2.46}$$

Deformation of a body is fully described if nine components (in 3-D space) of deformation tensor can be determined at any point of the body. The deformation tensor may be decomposed into strain tensor ε and rotation (deviatoric) tensor ω (Szostak-Chrzanowski et al. 2006):

$$\frac{\partial U_i}{\partial x_j} = \varepsilon_{ij} + \omega_{ij}, \tag{2.47}$$

where $\omega_{ij} = (1/2)((\partial U_i/\partial x_j) - (\partial U_j/\partial x_i))$ and ω_{ij} is skew symmetric: $\omega_{ij} = -\omega_{ji}$.

The stress–strain relations are mathematical descriptions of mechanical properties of the material using constitutive matrix. Linear elastic constitutive laws may model almost all materials subjected to sufficiently small loads. For linear elastic material, Hooke's law for a general anisotropic solid is given as: $\sigma_{ij} = E_{ijlm}\varepsilon_{lm}$, where E_{ijlm} represents components of the elasticity tensor and i, j, l, m have values 1, 2, 3. This is the so-called first constitutive equation (constitutive law). In real materials, complex transport equations must be solved to determine the time and spatial response of charges, for example, the Boltzmann equation or the Fokker–Planck equation or the Navier–Stokes equations with a general form:

$$F(\sigma_{ij}, \varepsilon_{ij}\, \varepsilon'_{ij}, T, t) = 0. \tag{2.48}$$

An entire physical apparatus for dealing with these matters has developed, such as linear response theory, Green–Kubo relations and Green's function (many-body theory). These complex theories provide detailed formulas for material parameters such as permittivities, permeabilities, conductivities, and so forth.

Constitutive Behavior

While there is rich diversity of structure at various levels in any piece of electronic packaging material, a fundamental assumption of continuum theory is to assume materials consist of aggregates of representative volume elements (RVE). The

deformation response of the material is then the result of the collective response of the RVEs. This is what is known as the constitutive behavior of the material. Such volume elements are large enough that material inhomogeneities can be ignored and average material property values can be used, but also small enough that it is entirely legitimate to apply the methods of mathematical analysis. In the case of electronic packaging and thermal managing materials, the constitutive behavior involves thermoelastic (silicon carbide die, encapsulant, ceramic and FR4 substrate, dielectric films, thermal interface materials [TIMs], etc.), elastic-plastic (metal films, traces, bonding wire, thermal managing materials), and viscoplastic/creep (solder, TIMs) behaviors.

The constitutive equation of thermoelastic behavior for anisotropic materials can be derived from (2.48):

$$\sigma_{ij} = C_{ijkl}(\varepsilon_{kl} - \alpha_{kl}\Delta T), \tag{2.49}$$

where C is a fourth-order tensor of elastic moduli, whose components are formed relative to the crystal lattice. C_{ijkl} is symmetric in indices i, j and k, l and generally has the following symmetry: $C_{ijkl} = C_{klij}$, assuming the existence of an elastic strain energy function. The number of independent components of C depends on the symmetry property of a particular crystal. If the crystal is isotropic, then there are only two independent elastic constants. For isotropic materials, $C_{ijkl} = \lambda\delta_{ij}\delta_{kl} + \mu(\delta_{ik}\delta_{jl} + \delta_{\mathrm{il}}\delta_{\mathrm{jk}})$, $\alpha_{ij} = \alpha\delta_{ij}$, and the following equations can be derived:

$$\sigma_{11} = \frac{E}{1+v}\left[\varepsilon_{11} + \frac{v}{1-2v}(\varepsilon_{11} + \varepsilon_{22} + \varepsilon_{33})\right] - \frac{\alpha E}{1-2v}\Delta T, \tag{2.50}$$

$$\sigma_{22} = \frac{E}{1+v}\left[\varepsilon_{22} + \frac{v}{1-2v}(\varepsilon_{11} + \varepsilon_{22} + \varepsilon_{33})\right] - \frac{\alpha E}{1-2v}\Delta T, \tag{2.51}$$

$$\sigma_{33} = \frac{E}{1+v}\left[\varepsilon_{33} + \frac{v}{1-2v}(\varepsilon_{11} + \varepsilon_{22} + \varepsilon_{33})\right] - \frac{\alpha E}{1-2v}\Delta T, \tag{2.52}$$

$$\sigma_{12} = \frac{E}{1+v}\varepsilon_{12}, \tag{2.53}$$

$$\sigma_{13} = \frac{E}{1+v}\varepsilon_{13}, \tag{2.54}$$

$$\sigma_{23} = \frac{E}{1+v}\varepsilon_{23}. \tag{2.55}$$

For elastic-plastic behavior, (2.48) transforms to $\sigma_{ij} = F(\varepsilon_{kl},T)$. The stress–strain relationship is nonlinear and depends on temperature T. Loading and unloading follow different stress–strain curves.

Creep is the plastic deformation of a material at a high homologous temperature below a material's yield stress. For creep behavior, (2.48) transforms to $\varepsilon_{ij} = F(\sigma_{kl},T,t)$. Creep can be subdivided into three categories primary, tertiary, and steady state creep. The qualitative behavior of the strain vs. time is shown in Figure 2.7. A material deforming by creep spends most of its time in the steady state region which is by far the dominant region when considering the effects of creep. The primary creep region is characterized by the following equation (Rhoads 2008):

$$\varepsilon_{\mathrm{pc}} = \beta t^{1/3}, \tag{2.56}$$

where β is a constant. Primary creep strain is usually less than 1% of the sum of the elastic, steady state, and primary strains. The mechanism in the primary region is the climb of dislocations that are not pinned in the matrix. The primary region is strongly dependent on the history of the material. If the material had been heavily worked before the creep test, there would have been many more dislocations present and the characteristics of the primary creep region would have been much different. When the amount of strain is high creep fracture or rupture will occur. In the tertiary region the high strains will start to cause necking in the material just as in the uniaxial tensile test. This necking will cause an increase in the local stress of the component which further accelerates the strain. Eventually the material will pull apart in a ductile fracture around defects in the solid. These defects could be precipitated at high temperatures or grain boundaries at lower temperatures. In any case the importance of the tertiary region to normal operation and creep design criteria is minimal. In Figure 2.7, the time scale of the tertiary region is greatly expanded for the purpose of clarity. Considering the small amount of time in addition to the fact that the tertiary region develops a plastic instability similar to necking, operating in the tertiary region is not feasible. Therefore, it is a conservative estimate to approximate the end of serviceable life of any component to

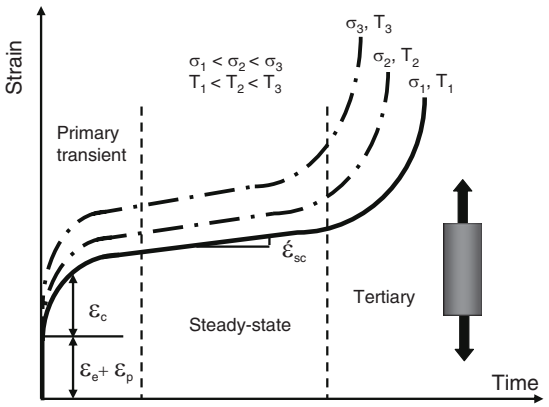

Fig. 2.7 Illustration of typical creep behavior

coincide with the end of the steady state creep region. The extra time in the tertiary region may be useful to consider only under accidental conditions.

The steady state region is so-called because the strain rate is constant. In this region the rate of strain hardening by dislocations is balanced by the rate of recovery. When the homologous temperature of a creep sample is between 0.3 and 0.7 of its melting temperature, the mechanism of creep is dislocation climb. This is the climb of dislocation jogs that impede the normal motion of the dislocation. This dislocation climb mechanism can be described by the following equation (Rhoads 2008):

$$\frac{\dot{\varepsilon}_{ss}}{\dot{\varepsilon}_0} = A\left(\frac{\sigma}{\sigma_0}\right)^m e^{-\frac{H}{kT}}, \tag{2.57}$$

where H is the activation energy for diffusion. A is a constant, and σ are the applied stresses. When higher temperatures are applied and the temperature is above 0.7 of the melting temperature, a different mechanism takes place. The creep is analogous to viscous flow in this region, and the mechanism of the creep is diffusion of atoms from one place to another. This type of creep can be described by (Rhoads 2008):

$$\frac{\dot{\varepsilon}_{ss}}{\dot{\varepsilon}_0} = \frac{1}{d_g^2}\frac{\sigma}{\sigma_0} e^{-\frac{H'}{kT}}, \tag{2.58}$$

where d_g is the diameter of the grains in the material, and H' is the diffusion activation energy. As grain size increases the creep rate decreases. In case for high temperature applications large grains are necessary to reduce the creep rate because they reduce the number of grain boundaries and increase the bulk diffusion distances.

Thermomechanical Analysis

The traditional use of prototypes to validate a new product design is rapidly being replaced by computational simulation. In fact, simulation driven design using virtual prototypes is currently being adopted by best in class manufacturers as the most consistent method to reduce time to market and hit their revenue, cost, launch date, and quality targets. For metal structures, simulation is now well established, but multimaterial structures incorporating ceramics and joints, like electronic packaging and its cooling system, pose a particular challenge. Thermomechanical analysis is one part of the computational simulation of the electronic packaging thermal products, which is based on the mathematical calculation and numerical simulation.

Plain Stress and Plain Strain

Many problems in thermomechanical analysis of electronic packaging and cooling systems can be treated by 2-D, or plane theory of elasticity. Plane stress and plane strain are two general types of problems involved in this plane analysis. Take a thin chip as an example, which is loaded by thermally induced forces applied along the boundary edges parallel to the plane of the chip. If the x–y plane is parallel to the plane of the chip, then the stress components σ_z, τ_{xy}, and τ_{yz} are zero on both plane faces and are assumed to be zero within the chip. The state of stress is then given by σ_x, σ_y and τ_{xy} and is so-called plane stress. Moreover, plane strain is more useful for packing thermal system. Consider a simple package assembly of a chip bonded to a heat spreader, the stresses that develop in the bond between the chip and the heat spreader when there is a temperature change applied to the assembly. For plane analysis, the assumptions are that any external forces acting do not vary with z and the strains ε_z, γ_{yz} and γ_{xz} on a section near the middle of the assembly are zero. In this case, Hook's law can be expressed as (Schmidt 2006):

$$\sigma_z = -v(\sigma_x + \sigma_y) - E\alpha\Delta T. \tag{2.59}$$

For σ_z, where thermal strain has been included, and the plane strain can be expressed (Schmidt 2006):

$$\varepsilon_x = \frac{1}{E}\left[\sigma_x(1 - v^2) - v(1 + v)\sigma_y\right] + (1 + v)\alpha\Delta T, \tag{2.60}$$

$$\varepsilon_y = \frac{1}{E}\left[\sigma_y(1 - v^2) - v(1 + v)\sigma_x\right] + (1 + v)\alpha\Delta T. \tag{2.61}$$

Beams and Laminate Assemblies

In some cases, electronic packaging and cooling system can be simplified as beams. The beam is a 3-D body, however, its length must be significantly larger than the depth (three or more times the depth). Internally, beams experience compressive, tensile and shear stresses as a result of the loads applied to them. As shown in Figure 2.8, one simple prismatic beam of length L will be considered, with an axial force F_x, transverse distributed load $p(x)$, and shear τ_0 as external force acting on the beam. For this beam, the stress σ_y and σ_z are zero and the normal stress σ_x and axial strain ε_x, based on the Hook's law (Schmidt 2006):

$$\sigma_x = \frac{F_x}{A} + \frac{My}{I}, \tag{2.62}$$

$$\varepsilon_x = \frac{F_x}{AE} + \frac{My}{EI} + \alpha\Delta T, \tag{2.63}$$

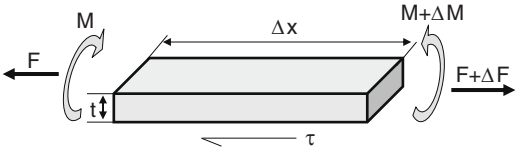

Fig. 2.8 Illustration of a free-body beam

where A is the cross-sectional area, y is the distance from the centroid of the cross section to any point on the cross section, M is moment, and I is the area moment of inertia about the z axis at the centroid of the cross section. When a strip is cut from a wide beam is under consideration, then a form of plane strain conditions exist and, for the strip, $\sigma_y = 0$ and $\sigma_z = v\,\sigma_x$, the strain becomes

$$\varepsilon_x = \frac{(1-v)F_x}{AE} + \frac{(1-v^2)My}{EI} + \alpha\Delta T. \tag{2.64}$$

Bimaterial Assembly

The typical bimaterial problems and solutions to simulate the electronic bonding system include bimaterial assembly axial effects, bimaterial assembly bending effects, and peeling stress.

The problem of bimaterial-axial effects is used to analyze two materials simply bonded together at their interface, as shown in Figure 2.9. Denote the top material layer by 1 and the lower material layer by 2, with the thickness, moduli, and coefficients of linear thermal expansion, designated by t_1, t_2, E_1, E_2, α_1 and α_2, respectively. A uniform temperature change, ΔT, in two materials is assumed. When $t_0 \to 0$, the bond property between two materials can be neglected, or does not influence the behavior of the system. Assuming the external force on the system is zero, therefore, $F = F_1 = F_2$. The radius of curvature R after the system experiences a temperature change can be related to the force F. The sum of the moments about z axis at $y = 0$ can be expressed as (Schmidt 2006):

$$M_{\mathrm{R}} = M_1 + M_2 - \frac{t_1 + t_2}{2}F = 0. \tag{2.65}$$

For a beam of unit width cut from the assembly, the moment curvature relation gives

$$M_i = \frac{E_i I_i}{\left(1-v_i^2\right)R} = \frac{E_i t_i^3}{12\left(1-v_i^2\right)R} = \frac{D_i}{R}, \quad i = 1, 2. \tag{2.66}$$

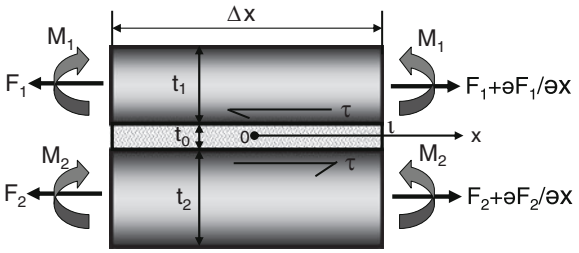

Fig. 2.9 Illustration of a bimaterials assembly (when bond thickness $t_0 \to 0$) or a bond assembly ($t_0 \ll t_1$ or t_2, and the bond is compliable)

where $D_{\mathrm{i}} = ((E_i t_i^3)/12(1 - v_i^2))$, the radius of curvature, R, for each member is assumed equal. This is valid if the strips are thin. Substituting (2.63) into (2.62), the relationship between R and material properties, thickness, and the force F can be obtained:

$$R = \frac{2(D_1 + D_2)}{(t_1 + t_2)F}. \tag{2.67}$$

On the other hand, the strains at the interface can be arisen due to the axial force, the bending moment, and the temperature change. If the strain at the lower surface of the upper member is equal to the strain at the upper surface of the low member when the system deforms, the strain compatibility condition will be meet (Schmidt 2006):

$$\frac{F}{E_1 t_1} + \frac{t_1/2}{R} + \alpha_1 \Delta T = -\frac{F}{E_2 t_2} - \frac{t_2/2}{R} + \alpha_2 \Delta T. \tag{2.68}$$

And a direct solution for the force F can be obtained by combining (2.64) and (2.65):

$$F = \frac{(\alpha_2 - \alpha_1)\Delta T}{\lambda}, \tag{2.69}$$

where

$$\lambda = \lambda_1 + \lambda_2 + \lambda_{12},\ \lambda_i = \frac{1 - v_i}{E_i t_i},\ \text{and}\ \lambda_{12} = \frac{(t_1 + t_2)^2}{4(D_1 + D_2)}.$$

This equation is the simplest form of solution for modeling electronic packaging and cooling system, but it is only valid away from edges of the strip because the force F was considered constant along the length. As the ends of the strip are approached, the force F must go to zero.

For the situation to assume that there is no significant bending, but the axial force does vary along the length, and therefore, the bond thickness $t_0 > 0$, as shown in Figure 2.9, and the shear force, τ, in the bond material, can be expressed as (Schmidt 2006):

$$\frac{\partial^2 \tau}{\partial x^2} - \frac{1}{K}(\lambda_1 + \lambda_2)\tau = 0, \tag{2.70}$$

where $K = t_0/G$. Let $k^2 = 1/K(\lambda_1 + \lambda_2)$, then (2.70) becomes

$$\tau = A \sinh kx + B \cosh kx, \tag{2.71}$$

Here, the coordinate system has its origin at the center of the assembly, and the assembly is symmetric about the origin. A and B can be solved by $\tau = 0$, at $x = 0$; and $K(\partial\tau/\partial x) = (\alpha_1 - \alpha_2)\Delta T$, at $x = l$. Therefore, (2.71) becomes (Schmidt 2006):

$$\tau = \frac{(\alpha_1 - \alpha_2)\Delta T}{Kk \cosh kl} \sinh kx, \tag{2.72}$$

when $x = l$, the maximum shear stress can be obtained:

$$\tau_{\max} = \frac{(\alpha_1 - \alpha_2)\Delta T}{Kk} \tanh kx. \tag{2.73}$$

In many situations, there is not a continuous bond between the chip and heat spreader, but only an edge bond. If the bond region begins at $x = c$, and ends at $x = l$, the shear stress can be expressed as (Schmidt 2006):

$$\tau = \frac{(\alpha_1 - \alpha_2)\Delta T[\sinh k(x-c) + kc \cosh k(x-c)]}{Kk[kc \sinh k(l-c)]}. \tag{2.74}$$

When the bending effect is included, the shear stress, τ, and the peeling stress (the stress normal to the interface), $p(x)$, can be derived (Schmidt 2006):

$$\tau = \frac{k(\alpha_2 - \alpha_1)\Delta T \sinh(kx)}{\lambda \cosh(kl)}, \tag{2.75}$$

$$p(x) = \frac{-a(\alpha_1 - \alpha_2)\Delta T \cosh(kx)}{K \cosh(kl)}, \tag{2.76}$$

where $k^2 = (\lambda_1 + \lambda_2 + \lambda_{12})/(K_1 + K_2 + K)$; $K_i = (2(1 + v_i)t_i)/3E_i = t_i/3G_i$ $i = 1, 2$; $D = D_1 + D_2$; $a = (D_1 t_2 - D_2 t_1)/2D$.

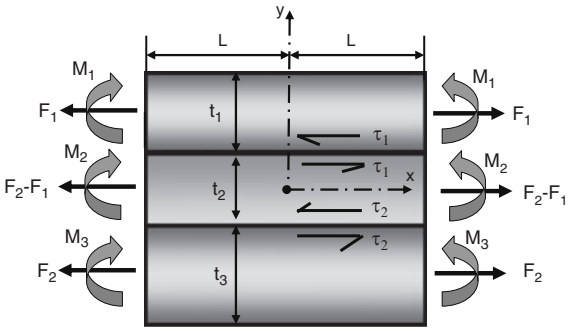

Fig. 2.10 Illustration of a tri-materials assembly

Trimaterial Assembly

The trimaterial assembly analysis can be used to simulate the three-layer electronic structure, such as a heat spreader, an adhesive or solder, and a chip. Figure 2.10 shows the model with three layers, designated as 1, 2, and 3, and a free-body diagram for a cut at some arbitrary x location. The approach is essentially the same as in the bimaterial assembly analysis, including (1) equilibrium is used to relate the radius of curvature to the axial forces, and then (2) the compatibility conditions at the interfaces are used to eliminate all unknowns except for the shear stress. This procedure is general and can easily be applied to any number of layers. The shear stress can be derived as (Schmidt 2006):

$$\tau_1 = k\Delta T[(\alpha_2 - \alpha_1)\beta_1 + (\alpha_3 - \alpha_2)\beta_2]\frac{\sinh(kx)}{\cosh(kl)}, \tag{2.77}$$

$$\tau_2 = k\Delta T[(\alpha_2 - \alpha_1)\beta_2 + (\alpha_3 - \alpha_2)\beta_1]\frac{\sinh(kx)}{\cosh(kl)}, \tag{2.78}$$

where $k^2 = (r \pm (r^2 - 4K_{12}K_{23}s)^{1/2})/2K_{12}K_{23}, r = \lambda_{12}K_{23} + \lambda_{23} + K_{12}, K_{ij} = K_i + K_j, \lambda_{20} = \lambda_2 - ((t_1 + t_2)(t_2 + t_3)/4)D, \lambda_{ij} = \lambda_i + \lambda_j + ((t_i + t_j)^2/4D), D = D_1 + D_2 + D_3$, and $s = \lambda_{12}\lambda_{23} - \lambda_{20}^2; \beta_1 = \lambda_{23}/(\lambda_{12}\lambda_{23} - \lambda_{20}); \beta_2 = \lambda_{20}/(\lambda_{12}\lambda_{23} - \lambda_{20}); \beta_3 = \lambda_{12}/(\lambda_{12}\lambda_{23} - \lambda_{20})$.

Numerical Method

The analytical approaches discussed previously are useful for assessing trends in the behavior of electronic components and provide useful insight into the behavior of an assembly. Once a preliminary design is developed for an assembly, extensive experimental prototyping and evaluation or numerical simulation should be done to make sure the device have the required reliability. Compared with experimental evaluation, numerical modeling and computer simulation have the advantage of

allowing changes in design without the prototype fabrication expense. As a numerical method, FEA has been successfully used in the simulation of electronic assemblies.

The FEA is a numerical technique for finding approximate solutions of PDEs as well as of integral equations. The solution approach is based either on eliminating the differential equation completely (steady-state problems), or rendering the PDE into an approximating system of ordinary differential equations, which are then solved using standard techniques such as Euler's method, Runge–Kutta, etc. The FEA method originated from the needs for solving complex elasticity, structural analysis problems in civil and aeronautical engineering. Its development can be traced back to the work by Alexander Hrennikoff in 1941 and Richard Courant in 1942. While the approaches used by those pioneers are dramatically different, they share one essential characteristic: mesh discretization of a continuous domain into a set of discrete subdomains, usually called elements. Hrennikoff's work discretizes the domain by using a lattice analogy while Courant's approach divides the domain into finite triangular subregions for solution of second order elliptic PDEs that arise from the problem of torsion of a cylinder. Courant's contribution was evolutionary, drawing on a large body of earlier results for PDEs developed by Rayleigh, Ritz, and Galerkin. Development of the finite element method began in earliest in the middle to late 1950s for airframe and structural analysis and gathered momentum at the University of Stuttgart through the work of John Argyris and at Berkeley through the work of Ray W. Clough in the 1960s for use in civil engineering. By late 1950s, the key concepts of stiffness matrix and element assembly existed essentially in the form used today and NASA issued request for proposals for the development of the finite element software NASTRAN in 1965. The method was provided with a rigorous mathematical foundation in 1973 with the publication of Strang and Fix's *An Analysis of The Finite Element Method*, and has since been generalized into a branch of applied mathematics for numerical modeling of physical systems in a wide variety of engineering disciplines, e.g., electromagnetism and fluid dynamics (Wikipedia 2009).

There have been a number of commercial FEA software packages available for application to mechanical and thermal design in electronic packaging, such as ABAQUS, ADINA, ANSYS, MSC/NASTRAN, and MARC. However, the drawback of the numerical analysis such as FEA is that there is no way to be sure the results are accurate. Therefore, caution must be used to always compare the compute results to estimates of the solution. Whenever possible, comparison to analytical results or experimental results is the best check.

Thermomechanical Failures

Thermomechanical failure is generally defined as any thermally induced change in the shape, material properties, or integrity of a part, which makes it incapable of performing its intended function. The failure of an electronic device can be the

result of one or any combination of responses of the device to loads and the environment. Failure mode seeks to predict failure conditions and correlate a calculated level of stress in the device with limits for the material obtained from tests of the material for each component.

Static Failure

The major static failure modes in the design of microelectronic components are ductile rupture and brittle rupture. Ductile rupture occurs when the plastic deformation in a material results in a progressive local reduction in cross-sectional area. This type of failure can occur in solder joints. Brittle failure occurs when the deformation results in a breaking apart of the interatomic bonds. Silicon and ceramics often fail by brittle fracture as a result of the thermal expansion mismatch between these materials and other bonded layers. The criteria for the ductile failure can be expressed as (Schmidt 2006):

$$S = \frac{\sqrt{2}}{2}[(\sigma_1 - \sigma_2)^2 + (\sigma_2 - \sigma_3)^2 + (\sigma_3 - \sigma_1)^2]^{1/2} \leq \sigma_{yP}. \tag{2.79}$$

When S is effective stress, σ_{yP} is the material yielding strength. If the value of S is less than σ_{yP}, then there is no yielding and the design can be considered adequate, otherwise, the design must be modified. The criteria for the brittle failure can be expressed as (Schmidt 2006):

$$|\sigma_1| < \sigma_u \quad \text{or} \quad |\sigma_3| < \sigma_u \quad \text{when } \sigma_1 < \sigma_2 < \sigma_3. \tag{2.80}$$

Brittle failure occurs when the materials no yielding and the stress–strain curve continues smoothly to fracture at ultimate stress σ_u. The failure can occurs rapidly with little or no indication of the impeding failure.

Failure of Fracture Mechanics

The theory of fracture mechanics is used to predict under what circumstances an existing imperfection, usually a crack, will propagate and eventually result in total failure. It uses methods of analytical solid mechanics to calculate the driving force on a crack and those of experimental solid mechanics to characterize the material's resistance to fracture. The term stress intensity K_{I} and the material fracture toughness are defined as (Lawn 1993):

$$K_{\mathrm{I}} = \sigma\sqrt{\pi a}, \tag{2.81}$$

and

$$K_c = \sqrt{EG_c} \quad \text{(for plane stress)}, \tag{2.82}$$

$$K_c = \sqrt{\frac{EG_c}{1-\nu^2}} \quad \text{(for plane strain)}, \tag{2.83}$$

$$G_c = \frac{\pi\sigma_f^2 a}{E}, \tag{2.84}$$

where K_I is the stress intensity, K_c the fracture toughness, ν is Poisson's ratio, σ_f is the stress at fracture, σ is the applied stress, a is half the crack length, and E is the Young's modulus. If $K_I < K_c$, the crack will not propagate; otherwise, the fracture will occur.

Fatigue Failure

Fatigue is the progressive and localized structural damage that occurs when a material is subjected to cyclic loading. The maximum stress values are less than the ultimate tensile stress limit, and may be below the yield stress limit of the material. Electronic components are frequently subjected to repeated or cyclic loads. Fatigue damage of the electronic component is usually nucleated at persistent slip band or preexisting defects on or near its free surface. A small crack may then form and grow into a major crack under cyclic loading. There major approaches have been developed and used to analyze and design against fatigue failure, including the stress-based approach, the strain-based approach, and the fracture mechanics-based approach.

Electronic components in a package or cooling system may be subjected to complex loadings so that the stress at a given point in the material often occurs in more than one direction. If sufficiently severe, such combined stresses can act together to cause the material to fail. A failure criterion that predicts failure when a certain combination of stresses reaches a limit, can be expressed as (Lawn 1993):

$$\bar{\sigma} = f(\sigma_1, \sigma_2, \sigma_3) < \sigma_c, \tag{2.85}$$

where $\bar{\sigma}$ is the effective stress, $f(\sigma_1, \sigma_2, \sigma_3)$ is a given function of the principle stress $\sigma_1, \sigma_2, \sigma_3$, and σ_c is a material property parameter. Historically, most attention has focused on situations that require more than 10^4 cycles to failure where stress is low and deformation primarily elastic.

In high-cycle fatigue situations, materials performance is commonly characterized by an *S–N* curve, also known as a Wöhler curve. This is a graph of the magnitude of a cyclical stress (S) against the logarithmic scale of cycles to failure (N). *S–N* curves are derived from tests on samples of the material to be characterized where a

regular sinusoidal stress is applied by a testing machine which also counts the number of cycles to failure. This process is sometimes known as coupon testing. Each coupon test generates a point on the plot though in some cases there is a runout where the time to failure exceeds that available for the test. Analysis of fatigue data requires techniques from statistics, especially survival analysis and linear regression.

In 1945, M.A. Miner popularized a rule that had first been proposed by A. Palmgren in 1924. The rule, variously called Miner's rule or the Palmgren–Miner linear damage hypothesis, states that where there are k different stress magnitudes in a spectrum, $S_i (1 \leq i \leq k)$, each contributing $n_i(S_i)$ cycles, then if $N_i(S_i)$ is the number of cycles to failure of a constant stress reversal S_i, failure occurs when (Schijve 2009):

$$\sum_{i=1}^{k} \frac{n_i}{N_i} = C. \tag{2.86}$$

C is experimentally found to be between 0.7 and 2.2. Usually for design purposes, C is assumed to be 1. This can be thought of as assessing what proportion of life is consumed by stress reversal at each magnitude then forming a linear combination of their aggregate.

Though Miner's rule is a useful approximation in many circumstances, however, it has two major limitations: (1) It fails to recognize the probabilistic nature of fatigue and there is no simple way to relate life predicted by the rule with the characteristics of a probability distribution. (2) There is sometimes an effect in the order in which the reversals occur. In some circumstances, cycles of low stress followed by high stress cause more damage than would be predicted by the rule. It does not consider the effect of overload or high stress which may result in a compressive residual stress. High stress followed by low stress may have less damage due to the presence of compressive residual stress.

Anderson, Gomez, and Paris derived relationships for crack growth with cycles N, in terms of the cyclical component ΔK of the stress intensity factor K (Schijve 2009):

$$\frac{\mathrm{d}a}{\mathrm{d}N} = C(\Delta K)^m, \tag{2.87}$$

where a is the crack length and m is typically in the range 3–5 (for metals).This relationship was later modified by Forman in 1967 to make better allowance for the mean stress, by introducing a factor depending on $(1 - R)$ where R = min. stress/max stress, in the denominator.

Where the stress is high enough for plastic deformation to occur, the account in terms of stress is less useful and the strain in the material offers a simpler description. Low-cycle fatigue is usually characterized by the Coffin–Manson relation (Schijve 2009):

$$\Delta\varepsilon_\mathrm{p} = 2\varepsilon_\mathrm{f}(2N)^c, \tag{2.88}$$

where $\Delta\varepsilon_p$ is the plastic strain amplitude; ε_f is an empirical constant known as the fatigue ductility coefficient, the failure strain for a single reversal; $2N$ is the number of reversals to failure (N cycles); c is an empirical constant known as the fatigue ductility exponent, commonly ranging from -0.5 to -0.7 for metals.

Based on these theories, the fatigue failure in electronic packaging and cooling system have been explored, however, majority of studies in this area are in its infancy and still experimental. Thus, the thermal fatigue limits of materials and structures are currently determined primarily based on the results of thermal cycling tests.

Analytical Techniques for Materials Characterization

Some analytical technical techniques, as summarized in Table 2.5, have been widely used to characterize materials employed in fabrication of electronic packaging and thermal management system. It is necessary to observe and obtain materials characteristics, such as composition, structure, morphology, and interface joining, in the synthesis, design, and development of electronic, photonic, and thermal modules, as well as in the analysis of their failure.

Optical Microscopy

Optical microscopy, or light microscopy, refers to the sample inspection with a type of microscope which uses visible light and a system of lenses to magnify images of small samples. A basic optical microscope has the following parts (Siliconfareast 2010): (1) a lamp to illuminate the specimen; (2) a nose piece to hold four to five objectives used in changing the viewing magnification; (3) an aperture diaphragm to adjust the resolution and contrast; (4) a field diaphragm to adjust the field of view; (5) an eye piece to magnify the objective image (usually by 10×); and (6) a stage for manipulating the specimen. During optical microscope inspection, the specimen is positioned perpendicularly to the axis of the objective lens. Light is then shown on the sample, which reflects some light back to the lens. The image seen in the microscope depends not only on how the specimen is illuminated and positioned, but on the characteristics of the specimen as well.

Optical microscopes are commonly classified as either low-power or high-power microscopes. Low-power microscopes are those which typically magnify the specimen at 5× to 60×, although some can magnify up to 100×. High-power microscopes, on the other hand, typically magnify the specimen at 100× to 1,000×.

There are three modes by which optical microscopy is commonly conducted, namely, brightfield illumination, darkfield illumination, and interference contrast. Brightfield illumination is the normal mode of viewing with an optical microscope. This mode provides the most uniform illumination of the sample. Under this

Table 2.5 Analytical techniques for material characterization

Technique	Incident probe	Analyzed phenomenon	Depth of analysis	Spatial resolution and detection limit	Applications
Optical microscopy	Visible light	Light reflection from surface microstructure	–	>2 μm –	Analyze samples in air or water, the images are in natural color with magnifications up to 1,000 times
X-ray diffraction	X-rays	Angles of X-rays relative to incident beam and sample that are diffracted by sample	100 Å to 1,000s Å	>10 μm 1%	Crystal structure, texture, orientation, phase analysis, element composition
Scanning electron microscopy	Electron beam	Electrons	Several nm to several μm	1–50 nm 0.1% weight	Morphology, topography, composition, and phases
Transmission electron microscopy	Electron beam	Electron beam passes through and interacts with the specimen	Several hundred nm	0.2 nm 0.1% weight	Morphology, topography, composition, and phases, microstructure and nanostructure
Scanning acoustic microscopy	Sound	Transducer and receiver	Several mm	Several μm	Cracks, delamination, voids
Atomic force microscopy	Atomic force	Atomic force	–	Fractions of nm	Nanoscale images

mode, a full cone of light is focused by the objective on the sample. The image observed results from the various levels of reflectivities exhibited by the compositional and topographical differences on the surface of the sample. Under darkfield illumination, the inner circle area of the light cone is blocked, such that the sample is only illuminated by light that impinges on its surface at a glancing angle. This scattered reflected light usually comes from feature edges, particulates, and other irregularities on the sample surface. Darkfield illumination is therefore effective in detecting surface scratches and contamination. Interference contrast makes use of polarized light that is divided by a Wollaston prism into two orthogonal light packets. These slightly displaced light packets hit the specimen at two different points and return to the prism through different paths. The differences in the routes of the reflected packets will produce interference contrasts in the image when the packets are recombined by the prism upon their return. Surface defects or features such as etch pits and cracks that are difficult to see under brightfield illumination can stand out clearly under Nomarski mode (Siliconfareast 2010).

The stereo microscope is designed differently from the compound optical microscopes, and serves a different purpose. It uses two separate optical paths with two objectives and two eyepieces to provide slightly different viewing angles to the left and right eyes, which produces a 3-D visualization of the sample being examined. Unlike compound microscopes, illumination in a stereo microscope most often uses reflected (episcopic) illumination rather than transmitted (diascopic) illumination, that is, light reflected from the surface of an object rather than light transmitted through an object. Use of reflected light from the object allows examination of specimens that would be too thick or otherwise opaque for compound microscopy. However, stereo microscopes are also capable of transmitted light illumination as well, typically by having a bulb or mirror beneath a transparent stage underneath the object, although unlike a compound microscope, transmitted illumination is not focused through a condenser in most systems. Stereoscopes with specially equipped illuminators can be used for dark field microscopy, using either reflected or transmitted light (Lipson et al. 1995).

Various video dual CCD camera pickups have been fitted to stereo microscopes, allowing the images to be displayed on a high-resolution liquid crystal display monitor. Software converts the two images to an integrated Anachrome 3-D image, for viewing with plastic red/cyan glasses, or to the cross converged process for clear glasses and somewhat better color accuracy.

X-Ray Diffraction

X-ray diffraction is a versatile, nondestructive analytical technique for identification and quantitative determination of the crystallographic structure, chemical composition, and physical properties of solid materials, powders, and thin films. The technique is based on observing the scattered intensity of an X-ray beam hitting

a sample as a function of incident and scattered angle, polarization, and wavelength or energy. Modern computer-controlled diffractometer systems use automatic routines to measure, record and interpret the unique diffractograms produced by individual constituents in even highly complex mixtures.

X-rays are only a small part of the electromagnetic spectrum with wavelengths (λ) ranging from 0.02 to 100 Å (Å = Angstroms = 10^{-8} m). X-rays used to study crystals have λ on the order of 1–2 Å (i.e., Copper $K\alpha = 1.5418$ Å). Visible light has much larger λs (4,000–7,200 Å) and thus, X-rays are much more energetic (i.e., can penetrate deeper into a material). This can easily be seen by inspection of the Einstein equation ($E = h\nu = hc/\lambda$; E is energy, ν frequency, c speed of light which is constant for electromagnetic radiation, λ wavelength, h Plank's constant).

Diffraction of an X-ray beam striking a crystal occurs because the λ of the X-ray beam is similar to the spacing of atoms in materials (1–10 Å). When an X-ray beam encounters the regular, 3-D arrangement of atoms in a crystal most of the X-rays will destructively interfere with each other and cancel each other out, but in some specific directions they constructively interfere and reinforce one another. It is these reinforced (diffracted) X-rays that produce the characteristic X-ray diffraction patterns that used for material identification.

W.L. Bragg (early 1900s) showed that diffracted X-rays act as if they were reflected from a family of planes within crystals. Bragg's planes are the rows of atoms that make up the crystal structure. These reflections were shown to only occur under certain conditions which satisfy the equation: $n\lambda = 2d \sin \theta$ (Bragg equation), where n is an integer $(1, 2, 3, \ldots, n)$, λ is the wavelength, d is the distance between atomic planes, and θ is the angle of incidence of the X-ray beam and the atomic planes. $2d \sin \theta$ is the path length difference between two incident X-ray beams where one X-ray beam takes a longer (but parallel) path because it reflects off an adjacent atomic plane. This path length difference must equal an integer value of the λ of the incident X-ray beams for constructive interference to occur such that a reinforced diffracted beam is produced. For a given λ of incident X-rays and interplanar spacing (d) in a material specimen, only specific θ angles will satisfy the Bragg equation (Gorring 1998).

Photographic plates were traditionally used to record the intensity and position of diffracted X-rays. Modern systems use diffractometers which are electronic X-ray counters (detectors) that can measure intensities much more accurately. Computers are used to process data and make necessary complex calculations. There are two main techniques to be discussed as below.

Single-Crystal Method

This method refers to X-ray beam is focused on a single crystal. Primary application is to determine atomic structure (symmetry, unit cell dimensions, space group, etc.). Older methods (Laue method) used a stationary crystal with white X-ray beam (X-rays of variable λ) such that Bragg's equation would be satisfied by numerous atomic planes. The diffracted X-rays exiting the crystal all have different θ and thus

produce spots on a photographic plate. The diffraction spots show the symmetry of the crystal.

Modern methods (rotation, Weissenberg, precession, four-circle) utilize various combination of rotating-crystal and camera setup to overcome limitations of the stationary methods (mainly the number of diffractions observed). These methods use monochromatic X-rays, but vary θ by moving the crystal mounted on a rotating stage. Usually employ diffractometers and computers for data collection and processing (Gorring 1998).

Powder Method

The powder method indicates an X-ray beam focused on a powder pellet or powder smeared on a glass slide, which is essential for materials that do not form large crystals (i.e., clays) and eliminates the problem of precise orientation necessary in single-crystal methods. This method is primarily used for material identification, and also can be used to determine material compositions (if d-spacing is a function of material chemistry) and to determine relative proportions of materials in a mixture. Monochromatic X-rays are focused on pellet or slide mounted on rotating stage. Because the sample is powder, all possible diffractions are recorded simultaneously from hypothetical randomly oriented grains. Mount is then rotated to ensure all diffractions are obtained (Gorring 1998).

X-ray powder diffractometry uses monochromatic X-rays on powder that is mounted on a glass slide that is attached to a stage which systematically rotates into the path of the X-ray beam through $\theta = 0$–90°. The diffracted X-rays are detected electronically and recorded on an inked strip chart. The detector rotates simultaneously with the stage, but rotates through angles 2θ. The strip chart also moves simultaneously with the stage and detector at a constant speed. The strip chart records the intensity of X-rays as the detector rotates through 2θ. Thus, the angle 2θ at which diffractions occur and the relative intensities can be read directly from the position and heights of the peaks on the strip chart. Then use the Bragg equation to solve for the interplanar spacing (d) for all the major peaks and look up a match with JCPDS cards (JCPDS refers to Joint Committee on Powder Diffraction Standards).

Powder diffraction is commonly used to identify unknown substances, by comparing diffraction data against a database maintained by the International Centre for Diffraction Data. It may also be used to characterize heterogeneous solid mixtures to determine relative abundance of crystalline compounds and, when coupled with lattice refinement techniques, such as Rietveld refinement, can provide structural information on unknown materials. Powder diffraction is also a common method for determining strains in crystalline materials. Thin film diffraction and grazing incidence X-ray diffraction may be used to characterize the crystallographic structure and preferred orientation of substrate-anchored thin films. High-resolution X-ray diffraction is used to characterize thickness,

crystallographic structure, and strain in thin epitaxial films. It employs parallel-beam optics. X-ray pole figure analysis enables one to analyze and determine the distribution of crystalline orientations within a crystalline thin-film sample. X-ray rocking curve analysis is used to quantify grain size and mosaic spread in crystalline materials.

In a summary, the angle of reflection of X-rays from a sample is related to the crystal structure and composition of the material. Typical X-ray analyses include lattice parameter measurements, crystallite size and distribution, texture analysis-preferred orientation of crystallites in a material, internal and residual stress measurements, CTE measurement, phase and composition identification, and film thickness measurements. The X-ray can penetrate into the sample with a depth of 100–1,000 Å, spatial resolution is more than 10 μm, and detection limit is 1%.

Scanning Electron Microscopy

The scanning electron microscope (SEM) is used to image the sample surface with much higher magnification than with an optical microscope by scanning it with a high-energy beam of electrons in a raster scan pattern. The electron beam interacts with the atoms that make up the sample producing signals that contain information about the sample's surface topography, composition and other properties such as electrical conductivity.

The SEM is not only an isolated instrument, but also represents a platform. When combined with scanning probe microscopy, the electron microscope can be used to further control manipulation of nanostructures or select an area for observation with high precision. In situ phase transitions can be seen when cryogenic or heating stages are installed in the chamber. The combination with a focused ion beam is used for specimen preparation in transmission electron microscopy (TEM). The types of signals produced by a beam of highly energetic (0.1–50 keV) electrons in SEM include the emission of secondary electrons, backscattered electrons (BSE), characteristic X-rays, photons, specimen current and transmitted electrons. Because the bombarding electron beam is scanned in the *X*–*Y* plane, an image for each of these different processes can be mapped with a suitable detector. A detector for secondary electrons, standard to all basic SEMs, records topography of the surface under observation with resolution on the order of 1–2 nm and magnification range from 10× to 500,000×. Due to the way these images are created, SEM micrographs have a very large depth of field yielding a characteristic 3-D appearance useful for understanding the surface structure of a sample. In addition, information on composition, phase, electrical, optical, thermal, and other properties can be mapped with excellent resolution with appropriate detectors. BSEs are beam electrons that are reflected from the sample by elastic scattering. BSEs are often used in analytical SEM along with the spectra made from the characteristic X-rays. Because the intensity of the BSE signal is strongly related to the atomic number of the specimen, BSE images can provide information about the distribution of different elements in

the sample. For the same reason, BSE imaging can image colloidal gold immunolabels of 5 or 10 nm diameter. Characteristic X-rays are emitted when the electron beam removes an inner shell electron from the sample, causing a higher energy electron to fill the shell and release energy. These characteristic X-rays are used to identify the composition and measure the abundance of elements in the sample (Schatten and Pawley 2007): (1) SEM-secondary and BSEs are detected from a sample with a focused primary electron beam, resulting in a surface image with a great depth of field; (2) EDX (Energy-Dispersive X-Ray Analysis)–The energy of X-rays emitted from a sample that is irradiated with the primary electron beam lead to elemental analysis and mapping; (3) high-resolution SEM imaging (1–50 nm), high-speed acquisition (30–60 s) with depth of analysis: few nanometers to few micrometers; (4) live SEM observation of the specimen in five to six orders of magnification (10× to 500,000×); (5) lateral resolution of EDX is ~0.5 μm, limit of detection ~0.1% weight, sample depth 0.02 μm; (6) nondestructive specimens; (7) vacuum compatibility required. Vacuum chamber accommodates specimens up to 100 mm in diameter; (8) versatility: multiple modes of operation available; and (9) readily accessible cross-sectional measurements.

Transmission Electron Microscopy

TEM is an imaging technique whereby a beam of electrons is transmitted through an ultrathin specimen, interacting with the specimen to produce a high-resolution image, magnified and focused by an objective lens and appears on an imaging screen, a fluorescent screen in most TEMs, plus a monitor, or on a layer of photographic film, or to be detected by a sensor such as a CCD camera. TEM is the most powerful electron microscope, with a resolving power 10 times better than that of a SEM and 1,000 times better than that of an optical microscope. A fine electron beam passes through the specimen, which must therefore be sliced extremely thinly–typically to about 100 nm. The TEM can resolve objects 0.001 μm (0.04 millionth of an inch) apart, a gap that is 100,000 times smaller than the unaided eye can see.

A TEM consists of a tall, evacuated column at the top of which is a heated tungsten filament that emits electrons. The beam of accelerated electrons are moved at uniform high velocity down the column by a high voltage (around 100,000 V) and pass through the slice of specimen at a point roughly half way down. Because the density of the specimen varies, the "shadow" of the beam falls on a fluorescent screen near the bottom of the column and forms an image. A camera is mounted beneath the screen to record the image. The electron beam is controlled by magnetic fields produced by electric coils, called electron lenses. One electron lens, called the condenser, controls the beam size and brightness before it strikes the specimen. Another electron lens, called the objective, focuses the beam on the specimen and magnifies the image about 50×. Other electron lenses below the specimen then

further magnify the image. On the screen a high-resolution image of the specimen can be viewed. The illuminated areas of the image correspond to those that have been hit by electrons which have passed through those areas of the specimen at which the electrons did not strike any solid material. The dark areas of the image correspond to those areas of the specimen, through which electrons could not pass through at all. At such points on the specimen, electrons have struck atoms of the specimen material and have been scattered.

The ultrathin layer of the specimen (some hundreds of nanometers thick), is first prepared properly, before being mounted on the microscope platform. Non-conductive specimen preparation entails drying it, embedding the specimen in plastic, and then coating it with gold or carbon, to facilitate conduction of electrons. The specimen is also stabilized. Further, the entire microscope assembly unit, inclusive of the specimen, is placed under vacuum to prevent the focused electron beam from getting scattered by air molecules. Cryogenic specimen preparation helps in better output. The whole microscope unit should be placed on the ground level to avoid influence of mechanical vibration on the image output (Raju 2010).

Typical applications of the TEM include: (1) observation of microstructure and nanostructure: size and morphology; (2) phase identification down to the nanoscale; (3) transmission electron diffraction; (4) double-tilt sample holders permit crystallographic studies, including defect analysis (dislocations, stacking faults, etc.); (5) chemical information discerned from emission of characteristic X-rays (energy dispersive spectroscopy of X-rays, or energy dispersive spectroscopy of X-rays [EDS]); (6) chemical information discerned from ionization edges in the electron energy loss spectrum (EELS); (7) high resolution imaging ($\sim$0.2 nm resolution); (8) formation of small electron probe allows diffraction, EDS, or EELS at the nanoscale; and (9) cross-section analysis (layer thickness, interface quality).

The specimens must be prepared as a thin foil, or etched so some portion of the specimen is thin enough for the beam to penetrate. Preparation techniques to obtain an electron transparent region include ion beam milling and wedge polishing. Materials that have dimensions small enough to be electron transparent, such as powders or nanotubes, can be quickly produced by the deposition of a dilute sample containing the specimen onto support grids. The suspension is normally a volatile solvent, such as ethanol, ensuring that the solvent rapidly evaporates allowing a sample that can be rapidly analyzed.

The imaging techniques are particularly important. Faults in crystals affect both the mechanical and the electronic properties of materials, so understanding how they behave gives a powerful insight. By carefully selecting the orientation of the sample, it is possible not just to determine the position of defects but also to determine the type of defect present. If the sample is orientated so that one particular plane is only slightly tilted away from the strongest diffracting angle (known as the Bragg angle), any distortion of the crystal plane that locally tilts the plane to the Bragg angle will produce particularly strong contrast variations. However, defects that produce only displacement of atoms that do not tilt the crystal to the Bragg angle (i.e., displacements parallel to the crystal plane) will not produce strong contrast.

Furthermore, the high-resolution transmission electron miscroscopy (HRTEM) technique allows the direct observation of crystal structure and therefore has an advantage over other methods in that there is no displacement between the location of a defect and the contrast variation caused in the image. However, it is not always possible to interpret the lattice images directly in terms of sample structure or composition. This is because the image is sensitive to a number of factors (specimen thickness and orientation, objective lens defocus, spherical and chromatic aberration), and although quantitative interpretation of the contrast shown in lattice images is possible, it is inherently complicated and may require extensive simulation of the images. Computer modeling of these images has added a new layer of understanding to the study of crystalline materials.

There are a number of drawbacks to the TEM technique. Many materials require extensive sample preparation to produce a sample thin enough to be electron transparent, which makes TEM analysis a relatively time consuming process with a low throughput of samples. Graphene, a carbon nanomaterial, relatively transparent, very hard and just one atom thick, is currently being used as a platform on which the materials to be examined are placed. Being almost transparent to electrons, a graphene substrate has been able to show single hydrogen atom and hydrocarbons. The structure of the sample may also be changed during the preparation process. Also the field of view is relatively small, raising the possibility that the region analyzed may not be characteristic of the whole sample. There is potential that the sample may be damaged by the electron beam, particularly in the case of plastic or biological materials.

Scanning Acoustic Microscopy

Scanning acoustic microscopy (SAM) is a nondestructive technique that can be used to image the internal features of a specimen or an integral structure. SAM can be used in microelectronic packaging and thermal management system for detecting popcorn cracking/delamination, die attach voiding, evaluating flip chip underfill integrity, and lid seal integrity in hermetically sealed packages, and detecting delaminations of submicron thickness, which are difficult to detect using X-ray radiography. Both delamination/cracking and die attach voiding are assembly related defects that can increase the susceptibility of components to failure in storage or use, although they may not constitute failures by themselves. Delamination and cracking can result in sheared or lifted wirebonds, passivation cracking, metallization shifting, intermittent electrical failures, and metallization/bond pad corrosion. Die attach voiding can lead to die cracking, die attach fracture, or thermal runaway due to poor heat dissipation through the die attach.

SAM works by directing focused sound from a transducer at a small point on a target object. Sound hitting the object is either scattered, absorbed, reflected (scattered at 180°) or transmitted (scattered at 0°). Typically, either the reflected or transmitted sound is gathered and measured. Based on the measurement, a value is assigned to the location investigated. The transducer is moved slightly and then

insonified again. This process is repeated in a systematic pattern until the entire region of interest has been investigated. Often the values for each point are assembled into an image of the object. The contrast seen in the image is based either on the object's geometry or material composition. The resolution of the image is limited either by the physical scanning resolution or the width of the sound beam, which in turn is determined by the frequency of the sound. A typical scanning acoustic microscope, for instance, may employ either pulse echo or through transmission inspection to scan for disbonds or delaminations. Pulse echo inspection consists of interpreting echos sent back by the package while through transmission inspection consists of interpreting the sound wave at the other end of the package, after it has passed through the latter. The ultrasonic wave frequency used usually ranges from 5 to 150 MHz. The sound wave may be generated by a piezoelectric crystal, or transducer, that has been cut to provide a specific frequency. It is activated by a high voltage pulse from a transmitter, which is also known as the pulser. The activation would cause the transducer to vibrate at the specified frequency, which transmits an ultrasonic wave through the package. This wave travels to the specimen through a medium or coupling, which is usually deionized water because sound waves could not travel through air at the frequencies used. The wave travels through the specimen's material at the material's velocity, with a portion of it being reflected back every time it hits an interface within the material. In the pulse echo method, the same transducer is used as sender and receiver of the sound waves. Pulses are repeated using repetition rates at which the echoes from one pulse will not interfere with those of another, for example, 10–20 KHz. The echoes received by the transducer are converted to voltages, amplified, digitized, and presented to the user as an image. In the through transmission technique, separate transducers are used to send and receive sound waves, both of which are on opposite sides of the specimen. The absence and presence of signals mean bad and good bonding, respectively (Siliconfareast 2010).

The resolution of a microscope can be defined as the minimum size of a feature that can be determined. The resolution of the light microscope is determined by the equation (Connor et al. 1998):

$$\omega = \frac{0.61\lambda_0}{N}, \tag{2.89}$$

which is based on the Rayleigh criterion. The resolution of the reflection acoustic microscope is somewhat better than the resolution based on the Rayleigh criterion and is given by the equation:

$$\omega = \frac{0.51\lambda_0}{N}, \tag{2.90}$$

where N is the numerical aperture and is equal to sin θ_0, which is the semiangle subtended. The wavelength, λ_0, is given by v_0/f, where v_0 is the velocity of sound in the fluid, and f is the frequency. A conservative estimate of the resolution of the acoustic scans can be between 90 and 180 μm.

As the frequency increases, the resolution improves but the depth of penetration decreases; thus, a tradeoff exists between improved resolution and depth of penetration. The best obtainable resolution is determined by the depth of penetration desired. The desired depth of penetration coupled with a minimum pulse length enables determination of the highest usable frequency. These factors are thus used to determine the best resolution (Connor et al. 1998).

Atomic Force Microscopy

The atomic force microscope (AFM) is a very high-resolution type of scanning probe microscope, with demonstrated resolution of fractions of a nanometer, more than 1,000 times better than the optical diffraction limit. The AFM is one of the foremost tools for imaging, measuring and manipulating matter at the nanoscale. The term "microscope" in the name is actually a misnomer because it implies looking, while in fact the information is gathered by "feeling" the surface with a mechanical probe. Piezoelectric elements that facilitate tiny but accurate and precise movements on electronic command enable the very precise scanning. The AFM was developed to overcome a basic drawback with STM (Scanning Tunneling Microscope), which can only image conducting or semiconducting surfaces. The AFM, however, has the advantage of imaging almost any type of surface, including polymers, ceramics, composites, glass, and biological samples.

The AFM consists of a microscale cantilever with a sharp tip probe at its end that is used to scan the specimen surface. The cantilever is typically silicon or silicon nitride (Si_3N_4) with a tip radius of curvature on the order of nanometers. When the tip is brought into proximity of a sample surface, forces between the tip and the sample lead to a deflection of the cantilever according to Hooke's law: $F = -kz$, where F is the force, k is the stiffness of the lever, and z is the distance the lever is bent. The force is not measured directly, but calculated by measuring the deflection of the lever, and knowing the stiffness of the cantilever. Depending on the situation, forces that are measured in AFM include mechanical contact force, van der Waals forces, capillary forces, chemical bonding, electrostatic forces, magnetic forces, Casimir forces, solvation forces, etc. Typically, the deflection is measured using a laser spot reflected from the top of the cantilever into an array of photodiodes. Other methods that are used include optical interferometry, capacitive sensing, or piezoresistive AFM cantilevers. These cantilevers are fabricated with piezoresistive elements that act as a strain gauge. Using a Wheatstone bridge, strain in the AFM cantilever due to deflection can be measured, but this method is not as sensitive as laser deflection or interferometry (Search 2010).

If the tip were scanned at a constant height, there would be a risk that the tip would collide with the surface, causing damage. Hence, in most cases a feedback mechanism is employed to adjust the tip-to-sample distance to maintain a constant force between the tip and the sample. Traditionally, the sample is mounted on a piezoelectric tube that can move the sample in the z direction for maintaining a

constant force, and the x and y directions for scanning the sample. Alternatively a "tripod" configuration of three piezo crystals may be employed, with each responsible for scanning in the x, y and z directions. This eliminates some of the distortion effects seen with a tube scanner. The resulting map of the area $s = f(x, y)$ represents the topography of the sample.

The AFM can be operated in a number of modes, depending on the application. In general, possible imaging modes are divided into static, also called contact modes and a variety of dynamic or noncontact modes (Wikipedia 2009):

Contact Mode

In constant force mode, the tip is constantly adjusted to maintain a constant deflection, and therefore constant height above the surface. It is this adjustment that is displayed as data. However, the ability to track the surface in this manner is limited by the feedback circuit. Sometimes the tip is allowed to scan without this adjustment, and one measures only the deflection. This is useful for small, high-speed atomic resolution scans, and is known as variable-deflection mode. Because the tip is in hard contact with the surface, the stiffness of the lever needs to be less than the effective spring constant holding atoms together, which is on the order of 1–10 nN/nm. Most contact mode levers have a spring constant of <1 N/m.

Lateral Force Microscopy

Lateral force microscopy measures frictional forces on a surface. By measuring the "twist" of the cantilever, rather than merely its deflection, one can qualitatively determine areas of higher and lower friction.

Noncontact Mode

Noncontact mode belongs to a family of AC modes, which refers to the use of an oscillating cantilever. A stiff cantilever is oscillated in the attractive regime, meaning that the tip is quite close to the sample, but not touching it. The forces between the tip and sample are quite low, on the order of pN (10^{-12} N). The detection scheme is based on measuring changes to the resonant frequency or amplitude of the cantilever.

Dynamic Force/Intermittant-Contact/"Tapping Mode" AFM

In this mode, a stiff cantilever is oscillated closer to the sample than in noncontact mode. Part of the oscillation extends into the repulsive regime, so the tip intermittently touches or "taps" the surface. Very stiff cantilevers are typically used, as tips

can get "stuck" in the water contamination layer. The advantage of tapping the surface is improved lateral resolution on soft samples. Lateral forces such as drag, common in contact mode, are virtually eliminated. For poorly adsorbed specimens on a substrate surface the advantage is clearly seen.

Force Modulation

Force modulation refers to a method used to probe properties of materials through sample/tip interactions. The tip (or sample) is oscillated at a high frequency and pushed into the repulsive regime. The slope of the force–distance curve is measured which is correlated to the sample's elasticity. The data can be acquired along with topography, which allows comparison of both height and material properties.

Phase Imaging

In phase-mode imaging, the phase shift of the oscillating cantilever relative to the driving signal is measured. This phase shift can be correlated with specific material properties that effect the tip/sample interaction. The phase shift can be used to differentiate areas on a sample with such differing properties as friction, adhesion, and viscoelasticity. The technique is used simultaneously with dynamic force mode so that topography can be measured as well.

The AFM has several advantages over the SEM. Unlike the electron microscope which provides a 2-D projection or a 2-D image of a sample, the AFM provides a true 3-D surface profile. Additionally, samples viewed by AFM do not require any special treatments, such as metal/carbon coatings, which would irreversibly change or damage the sample. While an electron microscope needs an expensive vacuum environment for proper operation, most AFM modes can work perfectly well in ambient air or even a liquid environment. In principle, AFM can provide higher resolution than SEM. It has been shown to give true atomic resolution in ultra-high vacuum. A disadvantage of AFM compared with the SEM is the image size. The SEM can image an area on the order of millimeters by millimeters with a depth of field on the order of millimeters. The AFM can only image a maximum height on the order of micrometers and a maximum scanning area of around 150×150 μm.

Another inconvenience is that an incorrect choice of tip for the required resolution can lead to image artifacts. Traditionally the AFM could not scan images as fast as an SEM, requiring several minutes for a typical scan, while an SEM is capable of scanning at near real-time (although at relatively low quality) after the chamber is evacuated. The relatively slow rate of scanning during AFM imaging often leads to thermal drift in the image, making the AFM microscope less suited for measuring accurate distances between artifacts on the image. However, several fast-acting designs were suggested to increase microscope scanning productivity including what is being termed video AFM (reasonable quality images are being obtained with videoAFM at video rate–faster than the

average SEM). To eliminate image distortions induced by thermodrift, several methods were also proposed (Search 2010).

AFM images can also be affected by hysteresis of the piezoelectric material and cross talk between the (x, y, z) axes that may require software enhancement and filtering. Such filtering could "flatten" out real topographical features. However, newer AFM uses real-time correction software (for example, feature-oriented scanning) or closed-loop scanners which practically eliminate these problems. Some AFM also uses separated orthogonal scanners (as opposed to a single tube) which also serve to eliminate cross-talk problems (Lipson et al. 1995).

Due to the nature of AFM probes, they cannot normally measure steep walls or overhangs. However, specially made cantilevers can be modulated sideways as well as up and down (as with dynamic contact and noncontact modes) to measure sidewalls, at the cost of more expensive cantilevers and additional artifacts.

Surface Finish Requirement and Contact Interface Compatibility

In the thermal management of electronic packaging, a proper material surface finish is usually required for the following reasons: (1) corrosion and oxidation protection for the base material of a component; (2) establishing a thermally or electrically conductive interface between two mating parts; (3) improving surface solderability; (4) maintaining galvanic compatibility between different contact materials. The surface finish is usually applied by electroplating; other processes such as painting, cladding or spraying also have been chosen for some specific applications.

Corrosion and Oxidation Protection

In many cases, thermal management materials are subject to corrosion in typical operating environments through oxidation, sulfidation or galvanic incompatibility, etc. Application of surface finish will seals off the thermal management components from the environment and therefore prevents corrosion. For this reason, the contact finish itself must be corrosion resistant, usually provided by noble metal finishes or by nonnoble metal finishes through forming passivating surface via tin or nickel plating for instance.

Noble Finish Selection

Noble finishes such as Au, Pd, and some alloys of these metals are intrinsically corrosion or oxidation resistant. When using this kind of finish, however, the extrinsic factors, such as contamination, base metal diffusion or intermetallic compound formation, and contact wear, would degrade their functions. Nickel

underplating is generally applied in providing such protection. Typical surface finish platings are 0.4–0.8 μm thick for the Au, or in some cases Au over Pd alloy, and 1.25–2.5 μm for the nickel underplating. These finishes vary in their degree of nobility and will be considered separately (Tong 2009).

Gold (Au)

Au provides an ideal contact surface finish due to its excellent electrical and thermal characteristics, as well as corrosion and oxidation resistance in virtually all environments. Pure gold, however, is relatively soft, therefore, alloyed gold plating is usually applied, with cobalt being the most common, at levels of a few tenths of a percent to increase the hardness and wear resistance (Tong 2009). Cost reduction objectives have led to the use of (1) selective plating practices such as reductions of plating area and thickness; (2) alternative noble metals, most commonly gold flashed palladium or palladium alloy.

Palladium (Pd)

Pd is not as good as gold in corrosion resistance or electrical/thermal conductivity. It is, however, significantly harder than gold, which improves durability performance. Palladium can catalyze the polymerization of organic deposits and result in contact resistance increase under fretting motions. Therefore, palladium is not as noble as gold although the effect of these factors on contact performance depends on the operating environment. In most applications, palladium is used with a gold flash (around 0.1 μm thick) to provide a gold contact interface (Tong 2009).

Noble Metal Alloys

Noble metal alloys mainly include gold alloys and palladium alloys. The major gold alloy used is 69 wt%Au–25 wt%Ag–6 wt%Pt. There are two palladium alloys in use, 80 wt%Pd–20 wt%Ni and 60 wt%Pd–40 wt%Ag. The Pd–Ni alloy is electroplated and the Pd–Ag finish is primarily an inlay. In general these finishes include a gold flash to counter the lower corrosion resistance of these alloys compared with gold. When applying these noble metal finishes onto thermal management materials, Ni underplating is usually used to provide benefits such as (Tong 2009): (1) Ni, through the formation of a passive oxide surface, seals off the base of porosities and surface scratches sometimes presented in the noble metal finished; (2) Ni provides an effective barrier against the diffusion of base metal constituents to the surface plating where the intermetallic compounds could be formed; (3) Ni provides a hard supporting layer under the noble surface which improves contact durability; (4) Ni provides a barrier against the migration of base metal to the surface finish, reducing the potential of the contact interface contamination due to the base metal

element migration. These benefits allow for equivalent or improved performance at reduced noble metal thickness. The effects of discontinuities are moderated, and the durability is improved. Ni underplating also allows a reduction in the size of the contact area which must be covered with the noble metal finish. All these functions serve to maintain the nobility of the contact surface finish at a reduced cost.

Nonnoble Finishes

Nonnoble contact finishes differ from noble finishes in that they always have a surface oxidation film, which can be disrupted during contact surface mating and the potential for recurrence of the films during the application life time of the contact thermal management components. Sn, Ag, and Ni are typical nonnoble finishes usually used. Sn is the most commonly used nonnoble finish; Ag offers advantages for high conductive contacts; and Ni is used in high temperature applications.

Tin (Sn)

The utilization of Sn surface finish derives from the fact that the oxide film is easily disrupted on mating, and metallic contact areas are readily established. Generation of a tin contact interface for tin finishes result from cracks in the oxide under an applied load. The load transfers to the soft ductile tin which flows easily, opening the cracks in the oxide, and tin then extrudes through the cracks to form the desired metallic contact regions. Here normal force alone may be sufficient; however, the wiping action that occurs on mating of contact spring gaskets for instance, virtually ensures oxide disruption and creation of a metallic interface. The potential problem with tin is the tendency for reoxidation of the tin at the contact interface if it is disturbed. This process is called fretting corrosion. The tin finish surface would be re-oxidized continuously when it is repeatedly exposed. The end of the result is a buildup of oxide debris at the contact interface leading to an increase in contact resistance. Driving force for fretting motions include mechanical (vibration and disturbances/shock) and thermal expansion mismatch stresses. Two approaches to mitigating fretting corrosion in tin and tin alloy finishes are high normal force (to reduce the potential for motion) and contact lubricants (to prevent oxidation). Each has been used successfully, and each has its limitations. High normal forces limit the durability capability of the finish, which is already low due to tin being very soft, and result in increased mating forces. Contact lubricants require secondary operations for application, have limited temperature capability, and may also result in dust retention (Tong 2009).

Another potential issue for tin plating finish is tin whisker growth. Tin whisker is an electrically conductive single crystal structure which spontaneously grows from the tin plating. Over time the whisker may grow to be several millimeters long. Whisker formation is usually identified as one of two mechanisms. (1) Spontaneous

whisker formation: the metal atoms forming the whisker diffuse through the deposit layer to the location from which the whisker then grows. In this case, they do not diffuse through any other phase layer. (2) Squeeze whisker formation is due to externally applied compressive stress. Whereas the growth rate of spontaneous whiskers can be up to 1 cm/year under the most favorable conditions, squeeze whiskers can grow at up to 1 m/year (Tong 2009). Tin whiskers are capable of causing electrical failures ranging from parametric deviations to sustained plasma arcing that can result in catastrophic short circuits. A great many attempts have been made to mitigate the effects of tin whisker growth. At this time, the only sure way of avoiding tin whiskers is not to use parts plated with pure tin for some critical applications. Compared with bright tin, matte tin is less prone to forming tin whisker. Even with matte tin plating, the whisker formation is still a majority concern especially for some critical applications. In general, 2–5 μm is the most dangerous tin plating thickness range for tin whisker growth. Below 0.5 μm and above 20 μm are the relatively safe ranges. For thicknesses below 1 μm and over 5 μm, tin whiskers are more resistant to grow. Examples of typical approaches to mitigate tin whisker formation include (Tong 2009): (1) solder dipping pure tin plated components using a leaded solder. The effectiveness of this approach at covering all pure tin plated surfaces can be variable. (2) Application of conformal coat material to pure tin plated surfaces. Conformal coat appears to reduce the growth rate of tin whiskers, but whiskers are still capable of growing through some conformal coat materials such as polyurethanes. (3) Plate or replate the component surfaces using finishes such as thicker matte tin (usually not less than 5 μm), tin/lead, nickel/tin or nickel which are substantially less prone to whisker formation.

Silver (Ag)

Silver can react with sulfur and chlorine to form silver sulfide and silver chloride films on its surface. Silver sulfide films tend to be soft and readily disrupted, and do not result in fretting corrosion. Silver chloride films, however, are harder, more adherent, and more likely to have detrimental effects on contact performance. In addition, silver is susceptible to electromigration, which can be a problem in some applications (Tong 2009). Therefore, silver has limited use in contact surface of thermal management components. Because of its high electrical and thermal conductivity and resistance to welding, however, silver finish still is a candidate for high conductive contacts. The thickness of silver finish is generally in the range of 2–4 μm.

Nickel (Ni)

Nickel plating forms a passivating oxide film that reduces its susceptibility to further corrosion. This passive film also has a significant effect on the contact

resistance of nickel. Because both nickel oxide and base nickel are hard, nickel finishes usually require higher contact normal forces to ensure the oxide film disruption. The self limiting oxide on nickel, however, makes it a candidate for high temperature applications. With the same mechanism as tin finishes, nickel contact finishes are also susceptible to fretting corrosion. When Ni underplating is covered with thin noble metal finishes for instance, wear-through of the finish due to mating cycles or fretting action, which exposes the nickel underplating, can result in fretting corrosion (Tong 2009).

Solderability of Surface Finishes

Solderability of some thermal management component surface finishes is required when the component needs to be soldered with other components. Solder bonds depend on whether the solder is either soluble in or capable of forming a metallic bond (a thin layer of intermetallic layer) with the material being soldered. Solderability requires that the metal surface finish be clean and remain clean and wettable by the solder with or without the aid of flux. Different metals have different affinity to a particular solder. Generally, tin plating is a most common surface finish that has an excellent solderability. However, the solderability can degrade over time. Loss of solderability in tin and tin alloy plating for instance, usually stems from three conditions: (1) excessive thickness of the intermetallic layer; (2) excessive amounts of oxides and other surface contaminants on the plating; (3) high levels of codeposited carbon from the organic brighteners in bright tin coatings. Each of these conditions can become worse over time: storage conditions, especially temperature can influence the rate of degradation and therefore shelf life of the plating. Therefore, the solderability of the surface finish needs to be inspected before soldering. Two most common methods used to predict and measure solderability of a surface finish are "dip and look" method and the wetting beam balance test. The dip and look test is performed according to JEDEC J-STD002A and a similar test using lead free solder. Parts are dipped in flux for 5 s and then immersed in the liquid solder for 5 s. The part is examined for the extent of solder wetting on the surface. If the wetting area is greater than 95% coverage of solder, the solderability of the surface finish is deemed acceptable. This is the test most commonly performed in the manufacturing environment to ensure on-going product solderability. The wetting beam balance test is another method used for solderability evaluation. In this test, the part is first fluxed and then partially submerged into a solder pot. During the submersion process, the force required to submerge the part is measured using a delicate balance. The insertion process produces a characteristic diagram of force vs. displacement with several key features which related to solderability. During insertion, the surface tension of the solder initially resists insertion by the terminal which appears as a downward dip in the curve. At some point, the solder begins to wet the surface of the terminal, drawing the terminal into the solder pot. The wetting force produces an upswing in the force curve. The first key metric is the

zero cross time. This indicates the time required for the wetting force to overcome the surface tension of the solder. Acceptability conditions vary, but generally times of less than 1 s are desired (Tong 2009).

Effects of Mating Cycles and Operating Environments on Contact Surface Finishes

The contact durability of some spring thermal management components depends on contact surface finish, the normal force, contact geometry and material's stress relaxation resistance. With respect to contact surface finish, the dominant factors of its durability performance include the hardness of the finish, contact geometry, normal force, surface roughness, and state of lubrication of the interface. Gold-flashed palladium or palladium alloy finishes provide the highest durability capability. Silver and tin finishes are severely limited in the number of mating cycles they can support. Contact lubricants are usually used to improve the mating cycle capability of noble finishes. An appropriate contact lubricant can improve the durability capability by an order of magnitude under favorable conditions. In addition, surface finish thickness largely affects the durability, with a roughly linear relationship between mating cycles and thickness for a given contact force/geometry configuration (Tong 2009).

Operating environments including temperature and corrosion severity will impact finish durability. The corrosion resistance of noble metal finishes decreases in the following order: gold, palladium, and palladium–nickel (80 wt% Pd–20 wt% Ni) alloy. The corrosion of the noble metal finishes are mainly caused by chlorine and sulfur. Nickel underplating is generally used to reduce the corrosion susceptibility of the noble metal coated parts. Tin finishes usually exhibit good stability with respect to corrosion, although fretting corrosion must always be taken into consideration for tin finishes. Temperature limitations for noble metal finishes exhibit a similar pattern to corrosion resistance. In both cases, the order is determined by the presence of the nonnoble constituent in the palladium alloys, because it is alloying elements that are susceptible to corrosion. Hard gold finishes, even though the alloy element is of the order of tenths of a percent, are also subject to oxidation as operating temperature increase. In general, soft, or pure, gold finishes are recommended for temperature above 125°C. Tin has a temperature limitation due to an increasing rate of intermetallic compound formation, a reduction in the already low mechanical strength and an enhanced oxidation rate. The interaction of these factors results in a recommendation that tin not be used above 100°C in conventional contact surfaces. Thermal cycling is another important environmental consideration and is arguably the major driving force for fretting corrosion of tin system. In addition, thermal cycling accelerates the effects of humidity on contact performance degradation (Tong 2009).

Galvanic Corrosion and Contact Interface Compatibility

Thermal management component design requires an understanding of galvanic corrosion and contact interface compatibility. Galvanic corrosion is the process by which the materials corrode in contact with each other. Three conditions must exist for galvanic corrosion to occur (Tong 2009): (1) two electrochemically dissimilar metals are in contact with each other; (2) an electrically conductive path presents between the two metals; and (3) a conductive path like electrolyte must be present for the metal ions to move from the more anodic metal to the more cathodic metal. If any one of these three conditions does not exist, galvanic corrosion will not occur. Usually when design requires that dissimilar metals come in contact, the galvanic compatibility is managed by plating or coating with other finishes.

Reliability Analysis and Environmental Performance Evaluation

The reliability of an electronic packaging and thermal cooling system indicates the probability that the system will be operational within acceptable limits for a given period of time. Advanced electronic packages are very complicated systems containing many thin layers, narrow conducting wires, and tiny solder joints. The dimensions of these structures are in the micrometer scale and getting smaller. Because of the fine features and large number of parts involved in each device, the probability of system failure is high unless high reliability of each device is ensured. In addition, more and more electronic packages are being used in very harsh environments, for instance, under-the-hood applications in automobiles, missiles stored in desert sand, airplanes flying in high attitude where temperatures can drop below negative 60°C, space stations exposed to strong radiation as well as extreme temperatures, etc. These harsh environments have imposed stringent requirements on the reliability of microelectronic systems. The packages must be designed to sustain high and low temperature extremes, to survive humid and corrosive surroundings, and to be protected from ultraviolet radiation. The mean time to failure for modern electronic packaging and thermal cooling system may range from several days to several decades at room temperature. Reliability tests cannot be performed for such long durations, but can simulate the real situation based on well-designed, well-understood, and thoroughly implemented accelerated testing. Reliability testing and simulating can be used to determine which failure modes apply to a given part, how probable it is that these failure modes will occur while the part is in service, and how they might be prevented during the design and manufacture of this part. Therefore, identifying and understanding the mechanisms that cause component failure is the key to make a reliable electronic packaging and thermal management system. In thermal reliability analysis, the focus is on the

failures caused by thermomechanical conditions that the electronic packaging and thermal cooling system experiences during manufacturing and service.

Failure Modes and Mechanisms

Failure Theories

Reliability is defined as the probability that a component functions as designed, whereas failure indicates the probability that a component does not perform the function any more. The fraction of a group of original devices that have failed at time t is called as the cumulative failure function, $F(t)$, while the fraction of a group of original devices surviving at time t is called the reliability function $R(t)$. Therefore, $R(t) = 1 - F(t)$. The failure rate, or the failure occurrences during a given time interval, $f(t)$ is defined as (Jha and Gupta 2003)

$$f(t) = \frac{\mathrm{d}F(t)}{\mathrm{d}t} = -\frac{\mathrm{d}R(t)}{\mathrm{d}t}, \tag{2.91}$$

$$F(t) = \int_0^t f(s)\mathrm{d}s. \tag{2.92}$$

The failure density $f(t)$ usually follows the bathtub curve. There is an initial high rate of failure due to manufacturing defect escapes; this stage is called infant mortality. After the initial failures, the majority of the remaining eligible products stay functional for its designed life. Towards the end, wearout starts to occur and there is a resurgence of high rate of failure indicating the end of useful life. The mean time to failure, MTTF $= \int_0^\infty tf(t)\mathrm{d}t$. Weibull distribution is commonly used to characterize the failure density (Jha and Gupta 2003):

$$f(t) = \frac{\beta}{\lambda}\left(\frac{t}{\lambda}\right)^{\beta-1}\exp\left[-\left(\frac{t}{\lambda}\right)^{\beta}\right], \tag{2.93}$$

where β is the shape parameter, a dimensionless number between 0.5 and 2.0. It is a measure of how the failure frequency is distributed around the average lifetime. λ is life time parameter, a measure of the average time-to-failure. It has unit of time and equals to the time at which 62.3% of the samples failed.

Chemical Failure Mechanisms

In an electronic package, corrosion of metallization and bonding region areas is the most common chemical failure mode. Corrosion is the result of two electrochemical reactions that occur when metal comes onto contact with an aqueous phase

containing dissolved ions. The anodic reaction process begins with the oxidation of atoms of a solid metal, changing their valence from zero to a positive number. This produces water-soluble metal ions that move into the aqueous solution, resulting in loss of the solid metal. The electrons liberated from the anodic reaction are then carried out of the metal phase by the cathodic reaction that uses these free electrons to reduce some species in the aqueous phase. For example, a region of the Cu surface as the anode, where oxidation occurs: Cu (s) $\rightarrow$ Cu^{+2}(aqueous solution) + $2e^{-}$. The electron given up by Cu reduces atmospheric oxygen to water at the cathode, which is another region of the same Cu surface: O_2 (g) + $4H^{+1}$ (aqueous solution) + $4e^{-}$ $\rightarrow$ $2H_2O$ (l). The Cu^{+2} ions are further oxidized by oxygen: $4Cu^{+2}$(aqueous solution) + O_2 $\rightarrow$ $2Cu_2O$ (s).

In addition, galvanic corrosion of metallization joints, moisture-induced corrosion, and stress corrosion of metallic constituents are the major chemical failure mechanisms in the electronic packaging and thermal cooling system.

Physical Failure Mechanisms

With increasing use of polymer materials in electronic packaging and thermal cooling system, physical aging of polymers has been one of the major failure modes. As physical aging is a gradual continuation of the glass transformation, many physical and mechanical properties of the polymer are affected in the same direction as during cooling through the T_g range. After aging, the polymer tends to become denser, stiffer, and more brittle; its yield strength may greatly be reduced; and its damping decreases and so does its creep rate.

Electromigration, a direct transport of atoms in a metal produced by an electric current, can be another failure mode especially when the electric current density is on the order of 10^4–10^5 A/cm^2 or higher. Electromigration-induced damage usually appears in the forms of voids and hillocks in thin-film conductors due to the massive atomic transport. Voids can grow and link together to cause electrical or thermal discontinuity in conductor lines or thermal dissipation systems. Hillocks can also grow and extrude out materials to cause short-circuit failure between adjacent conductor lines in integrated circuits.

Thermomechanical Failure Mechanisms

Electronic packaging and thermal cooling system are complicated material integrates operating under electrical, thermal and mechanical loading conditions. Many of these materials are organic materials that have highly nonlinear properties and that are very process and scale sensitive. These complex mechanical systems usually lead to complicated thermomechanical failure mechanisms, such as die or

other component cracking, adhesive delamination, solder fatigue failure, interconnection failure, and material fracture and interface voids.

Reliability Qualifications

To ensure product reliability, extensive reliability tests need to be performed during product development and before a new product can be shipped. Commonly accepted accelerated tests include thermal cycling and thermal shock, steady state thermal soaking, mechanical vibration, voltage extremes and power cycling, high humidity and high pressure, and combination of the above.

Thermal Cycling and Thermal Shock

The single, dual, and triple chamber can be used for temperature cycling. In single-chamber cycling, the load is placed in a stationary chamber, and is heated or cooled by introducing hot or cold air into the chamber. In dual-chamber cycling, the load is placed on a moving platform that shuttles between stationary chambers maintained at fixed temperatures. In triple-chamber temperature cycling, there are three chambers and the load is moved between them. This test is conducted to determine the ability of electronic packaging and thermal cooling system, including components and solder interconnects, to withstand mechanical stresses induced by alternating high and low temperature extremes. Permanent changes in electrical and/or physical characteristics can result from these mechanical stresses (JESD22-A104C). Typical testing conditions can be found from JESD22-A104C.

The thermal shock test is conducted to determine the resistance of a part to sudden exposure to extreme changes in temperature and to the effect of alternate exposures to these extremes. The conditions and recommended fluids can be found from JESD22-A106B.

Thermal cycling is an excellent test method for first order reliability assessment. However, it is not good for products with closely matched thermal coefficients of expansion because second-order effects, such as out-of-plane warpage, are not duplicated in this test method.

Comparability, power cycling, or powered functional cycling is similar to thermal cycling but more closely matches the actual service condition. It consists of a power-on transient in which the components go from room temperature to some steady-state temperature in a matter of minutes. This steady-state condition then lasts for several hours or longer before a power-off (cooling) transient occurs. The power-off condition then lasts for several hours. The transient conditions are difficult to determine either experimentally or analytically. For this test, the same support structure should be modeled as closely as possible. The same environment conditions, such as cooling air flow, should be duplicated. With such care this

approach will yield highly accurate reliability information. However, this method is more difficult, expensive, and time consuming.

Steady-State Temperature/Humidity Bias Life Test

The steady-state temperature humidity/bias life test is performed for the purpose of evaluating the reliability of nonhermetic packaged electronic devices in humid environments. It employs conditions of temperature, humidity, and bias which accelerate the penetration of moisture through the external protective material (encapsulant or seal) or along the interface between the external protective material and the metallic conductors which pass through it. The test requires a temperature–humidity test chamber capable of maintaining a specified temperature and relative humidity continuously, while providing electrical connections to the devices under test in a specified biasing configuration. Test conditions consist of a temperature, relative humidity, and duration used in conjunction with an electrical bias configuration specific to the device. The temperature of 85 $\pm$ 2°C (dry bulb) and relative humidity of 85 $\pm$ 5% should be applied to the entire useable test area. The wet bulb temperature is 81.0°C, and vapor pressure is 49.1 kPa, and the duration of 1,000 (-24, $+168$) hours applied continuously except during any interim readouts. The detail testing conditions can be found from EIA/JESD22-A101-B.

Mechanical Vibration

The vibration test is usually conducted in accordance with MIL-STD-167B. The vibration frequency is swept from 4 to 22 Hz. MIL-STD-167B requires an exploratory vibration test (10-min resonance survey sweep), a variable frequency test (5-min dwell at each frequency), and a 2-h endurance test at the resonant frequency.

Vibrating tables or shake tables are usually used to test electronic packaging and thermal cooling systems to determine or demonstrate their ability to withstand vibration. These machines are capable of producing three different types of vibration profile: sine sweep, random vibration, and synthesized shock. The part being tested will typically be instrumented with one or more accelerometers to measure how the component responds to the vibration input. A sine sweep vibration profile, for instance, typically starts vibrating at low frequency and increases in frequency at a set rate (measured in Hertz). The amplitude (measured in Gs) of the sine wave may increase or decrease as well. A sine sweep is intended to look for resonant frequencies in the part. A random vibration profile will excite different frequencies along a spectrum at different times. Significant calculation goes into making sure that all frequencies get excited to within an acceptable tolerance band. A random vibration test can be anything as short at 30 s up to several hours. It is intended to synthesize the effect of, for example, a car driving over rough terrain or a rocket taking off. A synthesized shock pulse is a short duration high level vibration calculated as a sum of many half-sine waves covering a range of frequencies. It is

intended to simulate the effects of an impact or explosion. A shock pulse test typically lasts less than a second.

References

Aller J (2007) Challenges of measuring thermal conductivity on deposited thin films and advantages of the 3-Omega method. http://courses.ucsd.edu/rherz/mae221a/reports/Aller_221A_F07.pdf. Accessed 03 March 2010.

An W (2002) Industrial applications of speckle techniques – measurement of deformation and shape. Ph.D. thesis. Royal Institute of Technology. Stockholm, Sweden. http://www.diva-portal.org/diva/getDocument?urn_nbn_se_kth_diva-3342-2__fulltext.pdf. Accessed 09 March 2010.

Anter (2007) Principal methods of thermal conductivity measurements. Technical Note #67. Anter Corporation. http://www.anter.com/TN67.htm. Accessed 01 March 2010.

Bourlon A J G (2005) Thermal conductivity measurement by the 3ω method. Technical Note PR-TN 2005/01035. Philips Electronics, Koninklijke.

Connor Z M, Fine M E, Achenbach J D, Seniw M E (1998) Using scanning acoustic microscopy to study subsurface defects and crack propagation in materials. JOM-e, http://www.tms.org/pubs/journals/JOM/9811/Connor/Connor-9811.html. Accessed 16 March 2010.

Gaal P S, Thermitus M-A, Stroe D E (2004) Thermal conductivity measurements using the flash method. J Therm Anal Calorim **78**:185–189.

Gorring M L (1998) X-ray diffraction. http://www.csam.montclair.edu/earth/eesweb/gorring/geos443/443notes/xray.html. Accessed 12 March 2010.

Heaney M B (1999) Electrical conductivity and resistivity. CRC Press LLC, Boca Raton, FL. http://www.autex.spb.ru/download/wavelet/books/sensor/CH43.PDF. Accessed 03 March 2010.

JEDEC (2004) Thermal shock. JESD22-A106B. JEDEC Solid State Technology Association, Arlington.

Jha N K, Gupta S (2003) Testing of digital systems. Cambridge University Press, Cambridge.

Kim I C (2007) Experimental investigation of size effect on thermal conductivity for ultra-thin amorphous poly methyl methacrylate (PMMA) films. M.S. thesis. Texas A&M University.

Krupke W F, Shinn M D, Marion J E, Caird J A, Stokowski S E (1986) Spectroscopic, optical, and thermomechanical properties of neodymium-and chromium-doped gadolinium scandium gallium garnet. JOSAB **3**(1):102–114.

Lawn B R (1993) Fracture of brittle solids, 2nd edn. Cambridge Solid State Science Series, Cambridge.

Lipson A, Lipson S G, Lipson H (1995) Optical physics. 3rd edn. Cambridge University Press, Cambridge.

Lu L, Yi W, Zhang D L (2001) 3ω Method for specific heat and thermal conductivity measurements. Rev Sci Instrum **72**:2996–3004. DOI:10.1063/1.1378340.

Lundgren U (2004) Characterization of components and materials for EMC barriers. PhD dissertation Lulea University of Technology, Sweden.

Maglić K D, Cezairliyan A, Peletsky V E (eds) (1984) Compendium of thermophysical property measurement methods. Vol. 1. Survey of measurement techniques. Plenum Press, New York.

Maglić K D, Cezairliyan A, Peletsky V E (eds) (1992) Compendium of thermophysical property measurement methods. Vol. 2. Recommended measurement techniques and practices. Plenum Press, New York.

Parker W J, Jenkins W J, Butler G P, Abbott G L (1961) Flash method of determining thermal diffusivity, heat capacity and thermal conductivity. J Appl Phys **32**:1679–1684

Post D, Han B (2009) Moiré interferometry. In: Sharpe Jr W N (ed) Springer handbook of experimental solid mechanics. http://www.springer.com/978-0-387-26883-5. Accessed 06 March 2010.

Raad P E, Komarov P L, Burzo M G (2005) An integrated experimental and computational system for the thermal characterization of complex three-dimensional submicron electronic devices. 11th THERMINIC, Belgirate, Italy, September 2005.

Raju A (2010) Transmission electron microscopy. http://www.sfermion.com/a253165-transmission-electron-microscopy.cfm. Accessed 12 March 2010.

Rhoads J L (2008) Basic explanation of creep processes. http://www.nuc.berkeley.edu/thyd/ne161/jlrhoads/creep.html. Accessed 10 March 2010.

Schatten H, Pawley J B (2007) Biological low-voltage scanning electron microscopy. Springer, New York.

Schijve J (2009) Fatigue of structures and materials, 2nd edn. Springer, New York.

Schmidt W F (2006) Mechanical design considerations. In: Ulrich R K and Brown W D (eds) Advanced electronic packaging, 2nd edn. Wiley, Hoboken.

http://www.search.com/reference/Atomic_force_microscope

Shinzato K, Baba T (2001) A laser flash apparatus for thermal diffusivity and special heat capacity measurements. J Therm Anal Calorim **64**:413–422.

http://www.siliconfareast.com/optical.html

http://sottosgroup.beckman.uiuc.edu/papers/stout.pdf

Symon K (1971) Mechanics. Addison-Wesley, Reading, MA.

http://www.fig.net/commission6/baden_2006/pdf/mod1/szostak-chrzanowski.pdf

Tong X C (2009) Advanced materials for electromagnetic interference shielding. CRC Press, Boca Raton.

Uher C (2005) Thermal conductivity of metals. In: Tritt T M (ed) Thermal conductivity: theory, properties, and applications. Springer, Berlin.

http://en.wikipedia.org/wiki/Finite_element_method

Zimprich P, Zagar B G (2007) Advanced laser speckle techniques characterize the complex thermomechanical properties of thin multilayered structures. Proc Estonian Acad Sci Eng **13**(4):394–408.

http://www.springer.com/978-1-4419-7758-8

Advanced Materials for Thermal Management of Electronic Packaging

Tong Ph.D, X.C.

2011, XXII, 618 p., Hardcover
ISBN: 978-1-4419-7758-8